Along-Strike Variation in the Shallow Velocity Structure beneath the Chenghai Fault Zone, Yunnan, China, Constrained from Methane Sources and Dense Arrays

Yunpeng Zhang[1,2], Hongfeng Yang[*3,4], Wei Yang[1,2], Weitao Wang[1,2], and Xiaona Ma[1,2]

Abstract

The fine structure of the fault zone and the surrounding area is the basis for understanding the process of earthquake nucleation and rupture propagation. To obtain the high-resolution structure of the Chenghai fault (CHF) and the nearby basins, we deployed two dense arrays and excited eight methane sources across the fault from October to November 2020. Based on the 611 *P*-wave travel times, we obtained the shallow velocity structure beneath the arrays using the simul2000 travel-time inversion program, and the results are as follows: (1) the shallow velocity structure beneath the CHF is very complex, with obvious velocity contrasts on both the sides of the regional fault; (2) low-velocity zones (LVZs) beneath the CHF show clear along-strike variations. The LVZs extend to ~500 m in depth with widths of ~2 km and ~5 km beneath the Qina and Pianjiao arrays, respectively, which are consistent with the Quaternary sediments, and the velocity contrasts along the interface of the LVZ can reach 20%–50%; and (3) the distribution of shallow surface tectonic geomorphology is mainly controlled by regional fault activities that are formed under the combined action of regional near-east–west stretching and clockwise rotation of microblocks. Our results can help improve cognition and seismic hazard assessment for potential earthquakes on the CHF, as well as lay the foundation for understanding the seismic wave velocity variation mechanism in the fault zone.

Cite this article as Zhang, Y., H. Yang, W. Yang, W. Wang, and X. Ma (2023). Along-Strike Variation in the Shallow Velocity Structure beneath the Chenghai Fault Zone, Yunnan, China, Constrained from Methane Sources and Dense Arrays, *Seismol. Res. Lett.* **XX**, 1–18, doi: 10.1785/0220230034.

Introduction

A fault zone is formed by the action of tectonic stress on different blocks, which is characterized by complex lithology, developed fissures, and damaged rocks (Evans and Chester, 1995; Ben-Zion and Sammis, 2003; Manighetti *et al.*, 2004; Li *et al.*, 2013; Goebel *et al.*, 2015; Choi *et al.*, 2016). The fault zone usually includes a low-velocity zone (LVZ) on the order of 100 m width (Yang, 2015), which can have significant impacts on the stress accumulation and release, as well as earthquake nucleation, deformation processes, and rupture propagation (Barr and Houseman, 1992; Chester *et al.*, 1993; Ampuero *et al.*, 2002; Wilson *et al.*, 2003; Manighetti *et al.*, 2007, 2009; Huang and Ampuero, 2011; Choi *et al.*, 2012; Li and Ghosh, 2016; Perrin *et al.*, 2016; Meng and Fan, 2021). The LVZ properties (e.g., width and depth extent) also have a significant impact on the earthquake size (Weng *et al.*, 2016) and amplify ground motion (Kurzon *et al.*, 2014; Song and Yang, 2022; Rosset *et al.*, 2022). Furthermore, the LVZ may not be uniform along a fault, and along-strike variations in LVZ properties have been revealed in different regions (e.g., Peng *et al.*, 2003; Lewis and Ben-Zion, 2010; Yang *et al.*, 2014; Zigone *et al.*, 2019; Shao *et al.*, 2022). For example, prominent LVZs of 200 m width were observed only in three out of five dense across-fault arrays beneath the San Jacinto fault in California (Yang *et al.*, 2014), showing a clear along-strike variation. Such along-strike variation in LVZs may have significant impacts on rupture propagation and site response. Therefore, high-resolution structures beneath the fault zone are critical for understanding the earthquake physics and estimating seismic hazards.

In the recent years, numerous studies have been conducted to image the fault zones using various methods based on the

1. Institute of Geophysics, China Earthquake Administration, Beijing, China, https://orcid.org/0000-0002-3907-8070 (YZ); 2. Key Laboratory of Earthquake Source Physics, China Earthquake Administration, Beijing, China; 3. Earth and Environmental Sciences Programme, Faculty of Science, The Chinese University of Hong Kong, Sha Tin, Hong Kong, China, https://orcid.org/0000-0002-5925-6487 (HY); 4. Shenzhen Research Institute, The Chinese University of Hong Kong, Shenzhen, Guangdong, China

*Corresponding author: hyang@cuhk.edu.hk

dense across-fault arrays, such as analysis of body-wave travel times from local and teleseismic earthquakes (Li *et al.*, 2007; Yang and Zhu, 2010; Qin *et al.*, 2018, 2021; Huang *et al.*, 2020; Yang *et al.*, 2020; Qiu, Ben-Zion, Catchings, *et al.*, 2021; Share *et al.*, 2022; Zhang *et al.*, 2022), observations and modeling of fault zone head waves, diffracted waves, trapped waves, and reflected waves (Li *et al.*, 1990; Ben-Zion and Malin, 1991; Peng *et al.*, 2003; Fohrmann *et al.*, 2004; Lewis *et al.*, 2005, 2007; McGuire and Ben-Zion, 2005; Cochran *et al.*, 2009; Yang and Zhu, 2010; Hillers *et al.*, 2014; Yang *et al.*, 2015; Qin *et al.*, 2018; Qiu, Ben-Zion, Catchings, *et al.*, 2021), travel time and ambient noise tomography (Lin *et al.*, 2013; Allam *et al.*, 2014; Hillers *et al.*, 2014; Taylor *et al.*, 2019; Zhang *et al.*, 2019; Zigone *et al.*, 2019; Yang *et al.*, 2020; Qiu, Niu, and Qin, 2021; Rost *et al.*, 2021), teleseismic receiver functions (Kahraman *et al.*, 2015; Jiang *et al.*, 2021), the spectral ratio from *P/S* waves of local and teleseismic earthquakes (Song and Yang, 2022), and the horizontal-to-vertical spectral ratio of both earthquake waveforms and noise (Huang *et al.*, 2020; She *et al.*, 2022; Chen *et al.*, 2023). However, accurately constraining the depth extent of the LVZ remains difficult. For example, in a study of the high-resolution structure of the Chenghai fault (CHF) in Yunnan, southwestern China, LVZ depth inverted from ambient noise tomography was overestimated, as shown in the overprediction of the teleseismic *S* arrivals (Yang *et al.*, 2020). Then, Jiang *et al.* (2021) obtained the *P*-wave velocity structure and a shallower LVZ depth using teleseismic receiver functions. Although the model can better fit the observed across-array delay times, they had to simplify the multilayered model to be one layer over a half-space, resulting in an average *S*-wave velocity. Furthermore, spectral ratio methods are only sensitive to width but not absolute depth (Song and Yang, 2022; She *et al.*, 2022). In addition, short-period dense arrays sit in the field for about 1–2 months, and depending on the background seismicity rate and data quality, there may not be sufficient good-quality seismic phases such as fault zone head waves, trapped waves, and reflected waves. Therefore, additional methods such as artificial sources could address the aforementioned problems.

An artificial source can be actively controlled in space and time according to the research requirements, and may be excited in high frequency to generate clear reflection and refraction phases. With the increasing limitations on the usage of explosives, many attempts have been made on electronic sparkers, hammering, vibroseis, airgun, methane source, and so on, to find an appropriate seismic source (Wang *et al.*, 2012, 2016; Chen *et al.*, 2017; Zhang, Wang, Lin, *et al.*, 2020; Zhang, Wang, Xu, *et al.*, 2020). In 2011, the world's first fixed airgun signal transmission station was established near the CHF in Binchuan, Yunnan, to understand the process of earthquake nucleation, and provide effective means for exploring the subsurface structure and monitoring the velocity variation (Wang *et al.*, 2012, 2020; Zhang *et al.*, 2017; Liu *et al.*, 2021; Luan *et al.*, 2022, 2023). However, airgun source depends on water bodies, making it inconvenient for exploring the fine structure of the fault zone. Other active sources have their limitations too. For instance, the propagation distance of the signal excited by electronic sparkers and hammering is short (Zhang, Wang, Lin, *et al.*, 2020), and the vibroseis is inconvenient to use in the junction of mountains and basins. Recently, a new type of artificial source (the methane source) has been proven to be environment friendly, efficient, safe, and economical. It produces seismic waves by rapidly releasing high-pressure air in borehole by igniting oxygen and methane with the reaction products of carbon dioxide and water, and can be applied to various complex terrains to detect small-scale subsurface structures, particularly in cities and fault zones (Wang *et al.*, 2019; Zhang, Wang, Lin, *et al.*, 2020; Xu *et al.*, 2021; Shao *et al.*, 2022). Therefore, combining a short-period dense array with the methane source enables us to conduct high-resolution imaging of shallow structures, with a short observation time.

In this study, we deploy two dense arrays across the central section of the CHF in the Binchuan and Qina basins of Yunnan, southwestern China (Fig. 1). Our study region is located in the northwestern Yunnan rift zone (NYRZ), which is near an arc-shaped turning point in the southeast of the Tethys–Himalayan tectonic domain. This region has been very active in the crustal movement because of the India–Eurasia collision, resulting in the formation of many rift basins in different scales, such as the Binchuan and Qina basins (Huang *et al.*, 2014; Luo *et al.*, 2015). These rift basins are populated areas, and the sedimentary layer can amplify seismic waves and significantly increase the earthquake damage (Kawase, 1996; Denolle *et al.*, 2014; Song and Yang, 2022). The CHF is a north–south-trending fault with both normal and left-lateral strike-slip motion (Huang *et al.*, 2014, 2018). Historically, large earthquakes with $M \geq 7.0$ have occurred at both the north and south ends, but no earthquake of magnitude 6.0 or greater has occurred in the central and southern sections in the past 200 yr (Luo *et al.*, 2015). Therefore, it has been considered a seismic gap.

So far, only one dense array has been deployed in the Zhoucheng sedimentary center across the southern side of the CHF (Yang *et al.*, 2020, 2021; Jiang *et al.*, 2021; She *et al.*, 2022; Song and Yang, 2022). Apparently, it cannot confirm whether there are along-strike variations. Furthermore, the depth extent of the LVZ using the passive source method is still controversial (Yang *et al.*, 2020; Jiang *et al.*, 2021; She *et al.*, 2022). Therefore, we deployed two additional dense across-fault arrays and conducted the methane source excitation experiment in the CHF from October to November 2020 (Fig. 1). In this study, we first describe the tectonic setting, dense array layout, and methane source excitation information. Then, we analyze the spectrum distribution of the methane source and pick up the first-arrival *P* waves. Finally, we perform high-resolution imaging using the simul2000 program

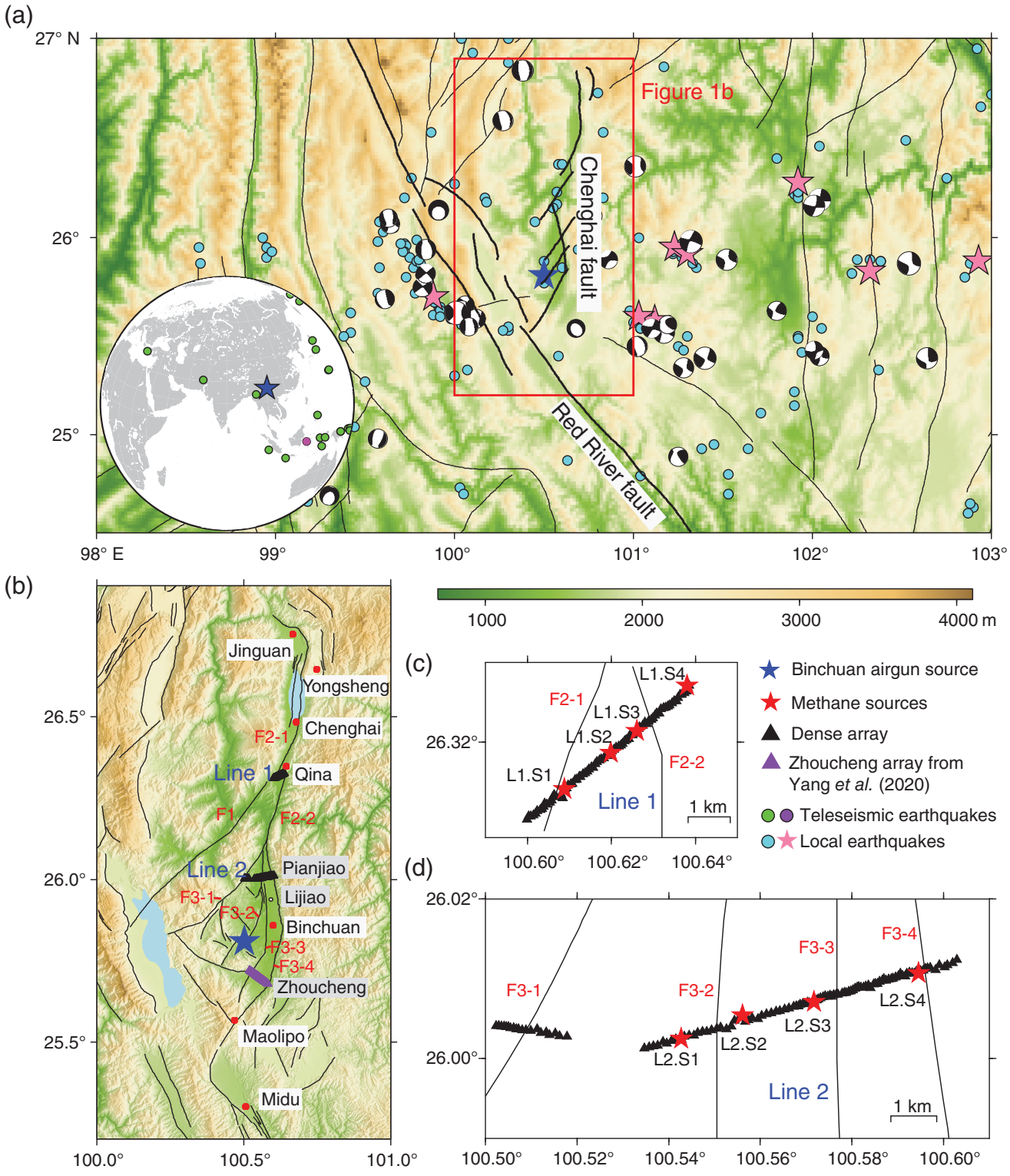

Figure 1. (a) Earthquakes (cyan dots, $M > 4$; and pink stars, $M > 6$) since 1970 (Dai and An, 2020) and faults in the study region. The focal mechanism plots show moment tensor solutions from the Global Centroid Moment Tensor (Global CMT) database. The blue star represents the airgun source in Binchuan. The green and purple dots in the inset figure represent the locations of teleseismic earthquakes with magnitudes larger than 5 during our dense array deployment. Waveforms of one earthquake (purple dot) are shown in Figure 9. (b) A zoom-in map showing the Chenghai fault and our line 1 and line 2 dense arrays (black triangles), in addition to the previous one (purple triangles, Yang *et al.*, 2020). The black lines represent the main faults (Deng *et al.*, 2003; Huang *et al.*, 2014, 2018, 2021; Luo *et al.*, 2015). F1, Zhoucheng-Qingshui fault; F2-1, Qina fault; F2-2, Jinjiang fault; F3-1 Shangcang-Yupeng fault; F3-2, Hequ-Shangying fault; F3-3, Hequ-Binju fault; and F3-4, Binchuan fault. (c,d) A further zoom-in view of the array geometries and methane source locations (red stars).

TABLE 1
Excitation Information of Methane Source in the Chenghai Fault

Shot	Wellhead Location (Relative to Sea Level)	Well Depth (m)	Injection Pressure (MPa)	Excitation Time (in Local Time, UTC + 8) (yyyy/mm/dd hh:mm:ss)	Lithology
L1.S1	100.60875079° E, 26.31412279° N, 1359.68 m	9.2	7.5	2020/11/05 03:16:55	Sandstone
L1.S2	100.61983091° E, 26.31864145° N, 1384.61 m	4	7.5	2020/11/05 04:11:44	Sandstone
L1.S3	100.62609522° E, 26.32139243° N, 1404.46 m	4	6	2020/11/05 05:51:58	Sandstone
L1.S4	100.63797829° E, 26.32707944° N, 1456.65 m	8.6	7.5	2020/11/05 05:04:38	Sandstone
L2.S1	100.54272160° E, 26.00251279° N, 1294.70 m	7	7.5	2020/11/05 23:10:11	Sandstone
L2.S2	100.55614239° E, 26.00540796° N, 1377.90 m	8.6	7.5	2020/11/05 00:26:25	Sandstone
L2.S3	100.57173303° E, 26.00714131° N, 1431.38 m	8.5	7.5	2020/11/05 01:16:40	Sandstone
L2.S4	100.59447724° E, 26.01070401° N, 1523.51 m	10	7.5	2020/11/05 02:02:44	Sandstone

(Evans *et al.*, 1994) along different segments of the CHF. Our results reveal that the velocity contrast and depth extent vary along the CHF.

Tectonic Setting and Dense Array Data

Tectonic setting

The CHF is a complex fault zone with a total length of ~200 km in the NYRZ and has developed multiple sets of fault segments with different strikes and activities, including north–south trending, northeast–southwest trending, and northwest–southeast trending (Fig. 1). The fault starts from the Jinguan basin in the north and presents a northwest–southeast trend, then turns into the north–south direction through Chenghai lake. It continues south, into the Binchuan basin and intersects with the Red River fault (Huang *et al.*, 2014). Many strong earthquakes have occurred in this region, such as the 1515 $M7^3/_4$ Yongsheng earthquake and the 2001 M_s 6.0 Yongsheng earthquake (Fan *et al.*, 2006; Luo *et al.*, 2015).

The CHF can be divided into six segments from north to south based on the difference in geometry and activity (Huang *et al.*, 2014, 2018, 2021; Luo *et al.*, 2015), including the Yongsheng–Jinguan segment, Chenghai segment, Qina segment, Binchuan segment, Maolipo segment, and Midu segment (Fig. 1). In the Qina segment, the Qina fault (F2-1) in the north branch and the Jinjiang fault (F2-2) in the south constitute the boundary of the Qina basin (a pull-apart rift basin), and both are dominated by left-lateral strike-slip with significant vertical activity. In the Binchuan segment, the Shangcang–Yupeng fault (F3-1) on the west boundary and the Binchuan fault (F3-4) on the east side formed a half-moon-shaped rift basin with both extensional and strike-slip properties.

Dense array

Studies have shown that fault zones with complex structures, particularly at the junction of two disconnected faults, are often areas with a high incidence of strong earthquakes (Huang *et al.*, 2014). Therefore, we select the Qina basin to deploy the line 1 dense array (also known as the Qina array), at the intersection of the Zhoucheng–Qingshui fault (F1), Qina fault (F2-1), and Jinjiang fault (F2-2).

A dense array (Yang *et al.*, 2020) has already been deployed on the southern side of the Binchuan basin (also known as the Zhoucheng array), located in the Zhoucheng Deposition Center (Fig. 1b). Considering the geological and geomorphological characteristics of the Binchuan basin, and the CHF, we select the roughly middle part of the Zhoucheng and Qina arrays to deploy the line 2 dense array (also known as the Pianjiao array), crossing the Shangcang–Yupeng fault (F3-1), Hequ-Shangying fault (F3-2), Hequ-Binju fault (F3-3), and Binchuan fault (F3-4).

The line 1 and line 2 dense arrays, respectively, consist of 80 and 120 Z-Land short-period three-component nodal seismographs (black triangles in Fig. 1), with a sampling rate of 500 points per second. The average station spacing is 50–100 m, and the instruments sit in the field for 35 days—from 26 October to 29 November.

Methane source

During the deployment of the dense array, a total of eight methane sources are excited along the two linear arrays (red stars in Fig. 1). The methane sources were buried in drill holes with depths of 4–10 m (Table 1), and can excite seismic waves by igniting oxygen and combustible gases (such as hydrogen, methane, etc.) with the reaction products of carbon dioxide and water (Wang *et al.*, 2019; Zhang, Wang, Lin, *et al.*, 2020; Xu *et al.*, 2021; Shao *et al.*, 2022).

The recent studies have shown that the seismic performance of methane sources varies under different excitation environments (Xu *et al.*, 2021). For example, the excitation energy is positively correlated with the injection pressure, but excessive

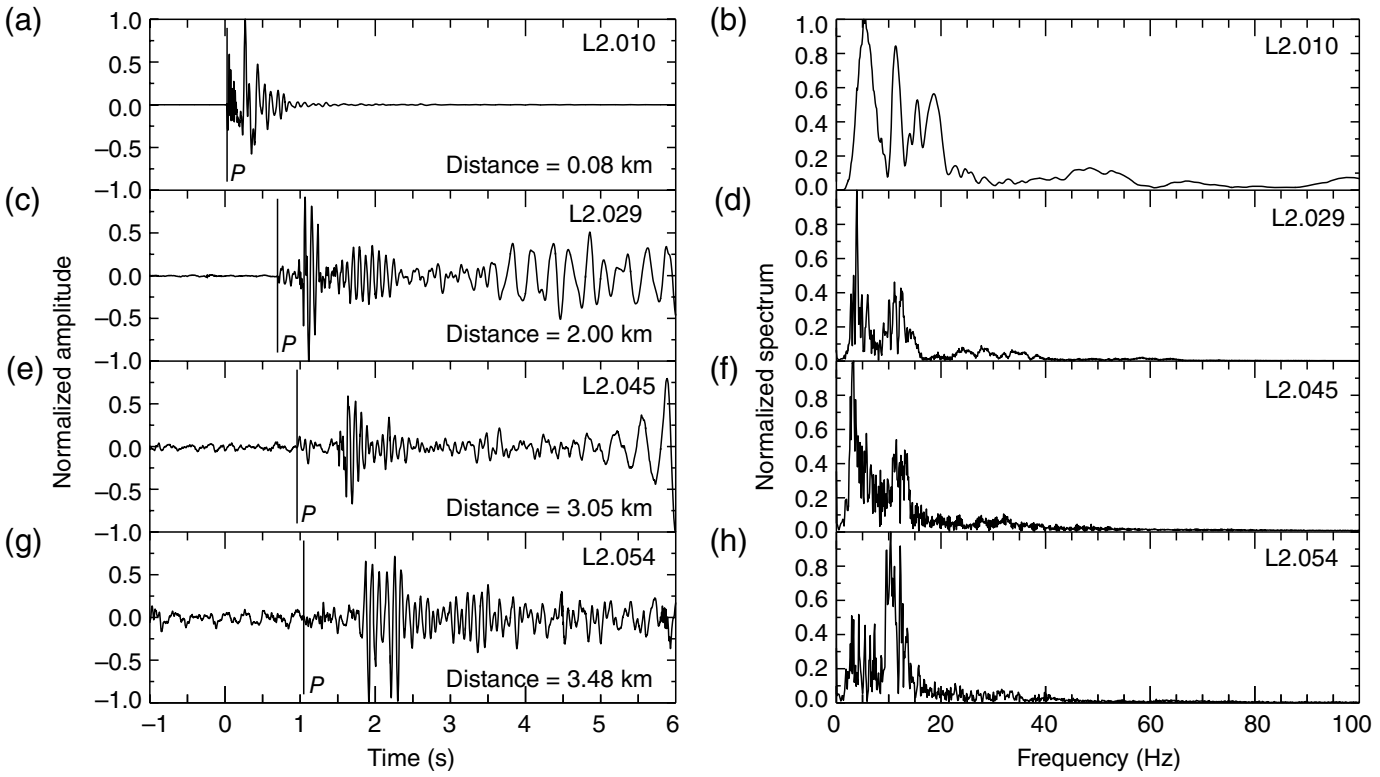

Figure 2. Raw waveforms of vertical components (a,c,e,g) and their spectrum (b,d,f,h) at different epicentral distances for the L2.S1 shot recorded on the line 2 array.

pressure can cause the seismic source device to directly spray out of the wellhead, posing a safety hazard. The excitation well depth should be increased as much as possible, and the excitation effect is better below the bedrock or water table. In addition, waveform recordings obtained during nighttime excitation usually have a higher signal-to-noise ratio (SNR). The energy difference of seismic signals excited under different environments could be large, but the frequency range is similar. For this experiment, the excitation location (relative to sea level), excitation time (local time in Beijing, China, UTC + 8), well depth, and injection pressure of the methane source are listed in Table 1. Z-Land seismometers were also deployed near each wellhead to record and verify the source information (e.g., the excitation time).

Data Analysis

Spectrum analysis of the methane source

To facilitate data processing, we first construct the original data into a unified Seismic Analysis Code (SAC) format database. Then, we obtain the three-component waveforms of the eight methane sources at each station according to the excitation time (−10 to 20 s).

Existing studies show that the dominant frequency of the methane source signal is 10–80 Hz (Wang *et al.*, 2019; Zhang, Wang, Lin, *et al.*, 2020). To obtain the waveform characteristics of the methane source in this study, we perform spectrum analysis on raw waveforms with different epicentral distances (Fig. 2). The spectrum characteristics show that the signal of the methane source is mainly distributed below 25 Hz, because the excitation location is located at the basin, and the seismic wave mainly retains the low-frequency components during propagation. Therefore, we apply a band-pass filter of 1–25 Hz to the waveform for further processing.

Phase picking

We manually pick *P*-wave arrivals from raw waveforms using the SAC software and then double-check the phases on the filtered data (1–25 Hz; Figs. 3 and 4). In total, 266 and 345 distinct *P*-wave phases are picked on line 1 and line 2, respectively.

As shown in Figures 3 and 4, signals from a single excitation have clear waveform records at a distance of more than 6 km. Taking the L2.S1 shot (Fig. 4a) as an example, the SNR of the methane signal is very high across the entire dense array. *P* and *S* waves overlap at small epicentral distances (<1.5 km); otherwise, the surface-wave signals are distinct. The amplitude of *S* waves becomes significantly higher than that of the *P* wave after crossing the basin (epicenter distance >1.5 km; Fig. 4a). When the epicentral distance exceeds 4 km, the waveform record becomes more complicated, with multiple groups of coherent phases (red dotted line in Fig. 4a) indicating the velocity variation at depths. Considering the relatively high precision and accuracy of *P*-wave phase picking, we perform tomographic studies on *P*-wave travel times in this study.

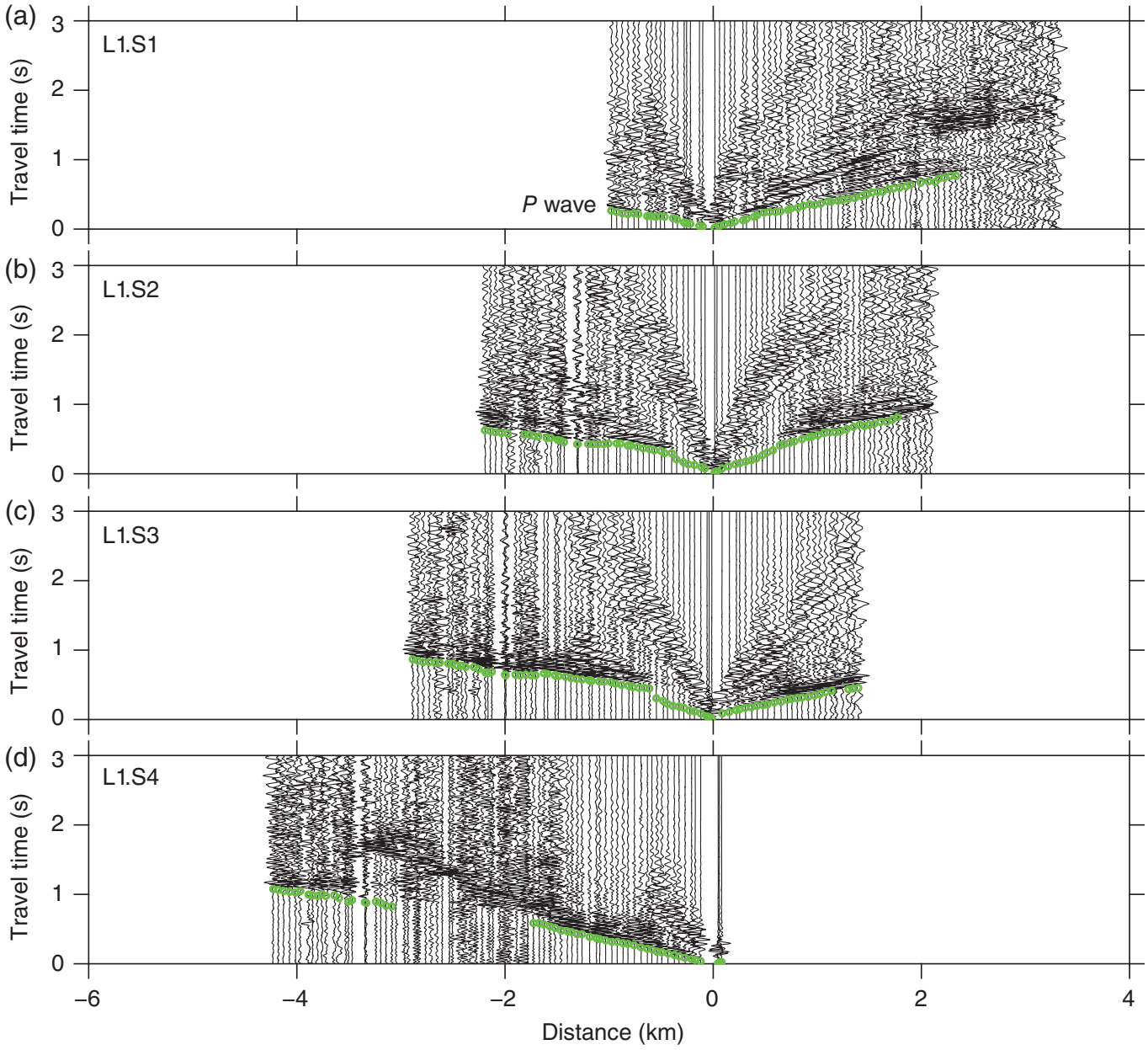

Figure 3. Vertical-component waveforms for the four shots (a–d) recorded on the line 1 array (filtered to 1–25 Hz). Each waveform is normalized according to its maximum amplitude. The green dots represent the picked *P*-wave phases.

Initial velocity model

We first invert the optimal 1D initial velocity model using the VELEST package (Kissling *et al.*, 1994; Kissling, 1995), which has been widely used to build initial models for 2D and 3D velocity inversion (e.g., Matrullo *et al.*, 2013; Zhang, Wang, Lin, *et al.*, 2020; Zhang, Wang, Xu, *et al.*, 2020).

By setting the vertical grids to 0.25 km, and varying the velocity (2.4–5.2 km/s) and gradient values at 1.5 km altitude, a total of 35 initial 1D velocity models are obtained as VELEST input models (gray lines in Fig. 5a and the specific velocity values are shown in Table 2). The inverted velocity models show similar distribution trends after 20 iterations of all 611 *P*-wave phases using different initial models (black line in Fig. 5a). We then average the black lines again as the VELEST input model to obtain a new velocity result, and this model is finally interpolated as the final initial velocity model (Fig. 5c).

Velocity Structure Inversion beneath the Dense Array

Inversion method of body-wave tomography

In this study, the simul2000 program (Evans *et al.*, 1994) is used for velocity inversion, which is widely applied in small-scale structural imaging studies (e.g., Thurber, 1983,

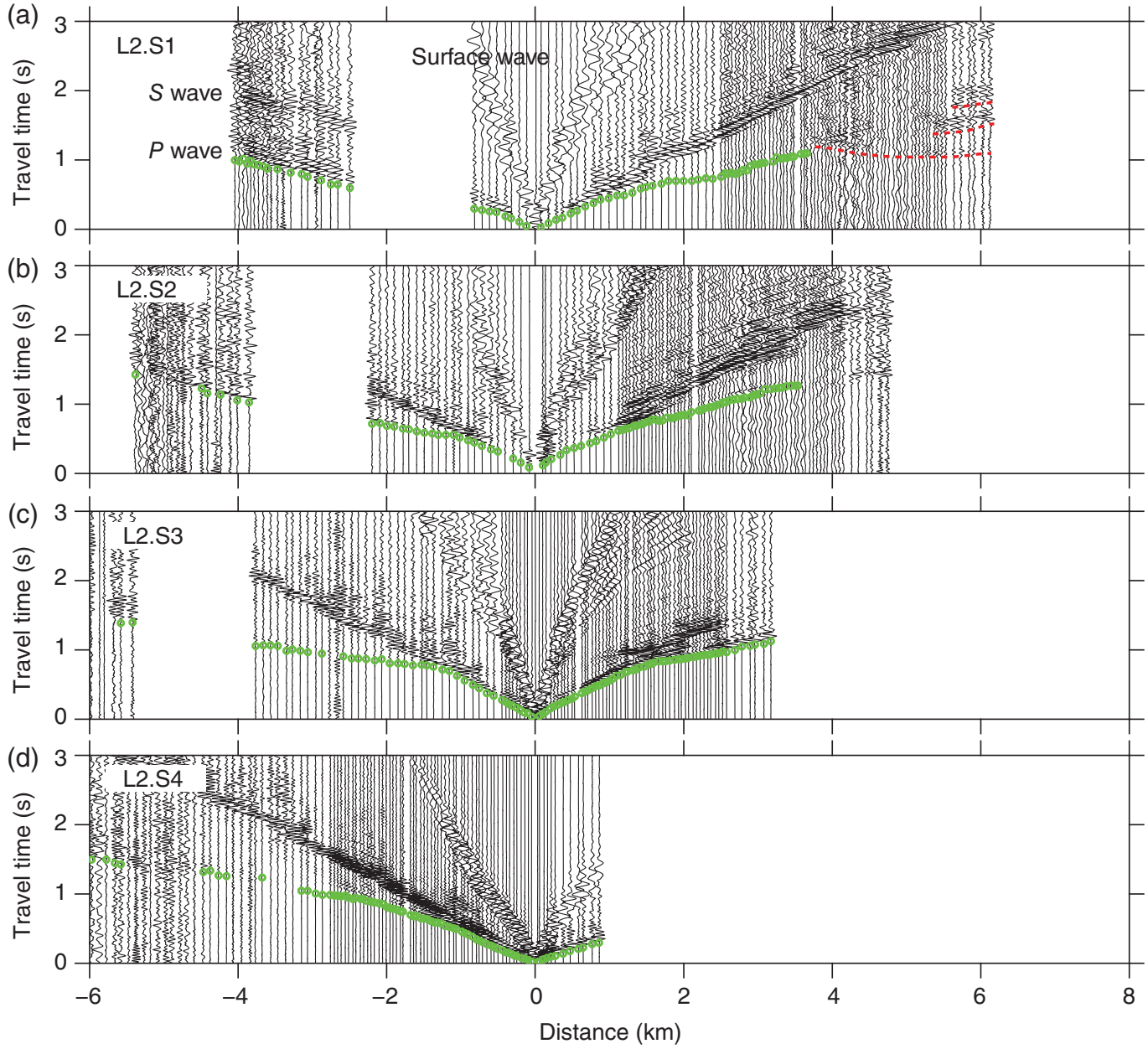

Figure 4. Vertical-component waveforms for the four shots (a–d) recorded on the line 2 array (filtered to 1–25 Hz). Each waveform is normalized according to its maximum amplitude. The green dots represent the picked *P* waves, and the red dotted lines represent the multiple groups of coherent phases.

1993; Thurber and Eberhart-Phillips, 1999; Lin *et al.*, 2014; Zhang, Wang, Lin, *et al.*, 2020; Zhang *et al.*, 2021).

The main principles of body-wave travel-time tomography used in the simul2000 program are as follows:

$$r_{ij}^{P} = t_{ij}^{\mathrm{obs}} - t_{ij}^{\mathrm{calc}}, \tag{1}$$

$$r_{ij}^{P} = \frac{\partial T_{ij}^{P}}{\partial x}\Delta x + \frac{\partial T_{ij}^{P}}{\partial y}\Delta y + \frac{\partial T_{ij}^{P}}{\partial z}\Delta z + \Delta\tau_i + \sum_{l=1}^{L}\frac{\partial T_{ij}^{P}}{\partial m_l^{P}}\Delta m_l^{P}, \tag{2}$$

in which t_{ij}^{obs}, t_{ij}^{calc}, and T_{ij} are the observed *P*-wave travel time, calculated travel time, and travel time from event i to station j, respectively. The r_{ij}^{P} is the *P*-wave arrival-time residual. τ_i and (x, y, z) are the origin time and location of the earthquake, respectively. m_l^{P} is the *P*-wave velocity of the lth grid, and Δ denotes the perturbation from its initial value. The simul2000 program adopts the damped least-squares method to invert the velocity perturbations, and the effect of topography (e.g., station elevation) is considered when doing ray tracing (Evans *et al.*, 1994; Lin *et al.*, 2014).

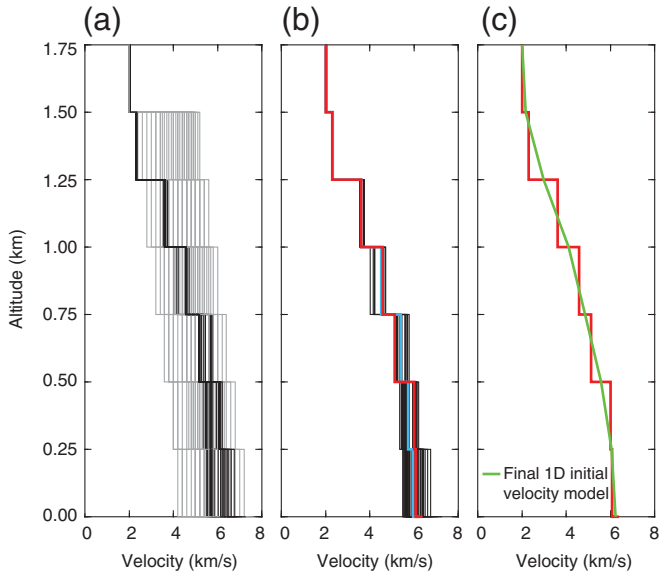

Figure 5. Optimal initial velocity model inverted from the VELEST package. (a) Starting input models (gray lines and the specific velocity values are shown in Table 2) with different gradients and the inverted models (black lines) from VELEST package. (b) The average velocity (blue line) of the black lines and the corresponding inverted model (red line) after the VELEST. (c) The final 1D initial velocity model (green line) used for tomography.

Optimal selection of inversion parameters

When using simul2000 for velocity inversion, the initial 1D velocity model is derived from the VELEST result (green line in Fig. 5). The origins of line 1 and line 2 are set near the L1.042 station (near the center of line 1) and L2.E035 station (near the east center of line 2), respectively. Considering the length and station spacing of the dense array, horizontal grids are finally set to 0.3 km × 0.3 km and 0.5 km × 0.5 km for line 1 and line 2 respectively. Vertical grids are both set to 0.25 km (Fig. 6).

Damping parameters are important in the inversion, and are usually selected through a tradeoff analysis between data misfit and model variance by searching various damping values (Lin *et al.*, 2014; Zhang, Wang, Lin, *et al.*, 2020; Zhang, Wang, Xu, 2020; Zhang *et al.*, 2021). We only invert the velocity model because the methane source has an accurate excitation time and location. Using the first-arrival *P*-wave phases picked up on line 1 and line 2, we explore a wide range of damping values (1–9000) to obtain the relationship between model variance and data misfit (Fig. 6). The damping parameters of V_P for line 1 and line 2 are set to 15 and 60, respectively, based on the *L*-curve distribution.

Resolution test and velocity inversion result

The tomographic inversion is converged after 9 and 16 iterations for line 1 and line 2, respectively. In addition, the root mean square of the travel-time residual is reduced by 66% and 69% from 0.080 and 0.154 s to 0.027 and 0.048 s, respectively. Before the inversion, the *P*-wave travel-time residuals are mainly distributed in −0.2 to 0.4 s, whereas the residuals show a Gaussian distribution within −0.1 to 0.1 s centered at 0 s after the inversion (Fig. 7).

Checkerboard resolution test is also performed to evaluate the model quality. The excitation locations, source–receiver pairs, grid points, and inversion parameters are all kept the same as for real data inversion. Synthetic travel times are computed using the 1D initial model (green line in Fig. 5) with alternative ±5% velocity perturbations across two adjacent grid nodes. The *P*-wave velocity structure and checkerboard results beneath the line 1 and line 2 dense arrays are shown in Figure 8, respectively. Except for the relatively poor ray distribution on the west side of line 2 due to the lack of methane source (not drawn in the article), the *P*-wave velocity structure has a good resolution in the study area from 0 to 1.5 km at depth.

Distinct LVZs are observed beneath both the line 1 and line 2 dense arrays, and appear to be mainly controlled by regional fault zones (Fig. 8). Located at the boundary of LVZs, the Qina fault (F2-1), Jinjiang fault (F2-2), and Binchuan fault (F3-4) have significant velocity contrasts in both the sides, which can reach 0.5–2 km/s. Inside the LVZs, velocity differences also exist, such as low–high–low velocity distribution with slight variation beneath the Hequ–Binju fault (F3-3).

Yang *et al.* (2020) used an *S*-wave velocity of 1.2 km/s from ambient noise tomography result to constrain the width and depth of the LVZ beneath the Zhoucheng dense array on the southern side of the Binchuan basin (Fig. 1b), and Jiang *et al.* (2021) revealed that the average V_P/V_S beneath this array is 2.12 using a newly developed receiver function inversion technique. Similar to Yang *et al.* (2020), we used 2.5 km/s to delineate the range of the *P*-wave LVZ. Beneath the line 1 (Qina array), the average *P*-wave velocity inside the LVZ is ∼2.0 km/s, and the average velocities on the southwest and northeast sides are ∼4 and ∼3 km/s with ∼50% and ∼33% reduction, respectively (Fig. 8a). The velocity beneath the line 2 (Pianjiao array) is also faster on the southwestern side of the LVZ than that on the northeast. Within the LVZ, V_P is ∼2.0 km/s, whereas the average velocities of the *P* wave on the southwestern and northeastern sides of the LVZ are ∼3.0 and ∼2.5 km/s with ∼33% and ∼20% reduction, respectively (Fig. 8c). In addition, the LVZ width beneath the Qina and Pianjiao arrays is ∼2.0 and ∼5.0 km, respectively, and both the depths extend to ∼500 m (Fig. 8a,c).

Based on the previous research on the Zhoucheng array, Yang *et al.* (2020) found that the V_S is ∼600 m/s within the LVZ, with ∼60% and ∼40% reductions compared to the northwestern and southeastern sides of the LVZ, and the LVZ is 3.4 km in width and can extend to ∼1.5 km in depth. Jiang *et al.* (2021) and She *et al.* (2022) show that the LVZ extends to ∼1.1 and ∼1.0 km in depth using receiver functions and spectral ratio methods, respectively. The depth extents of

TABLE 2
Specific Velocity Values for VELEST Input Models

Depth (km)	1.50	1.25	1.00	0.75	0.50	0.25	0.00	Depth (km)	1.50	1.25	1.00	0.75	0.50	0.25	0.00
Model 1	4.50	4.60	4.70	4.80	4.90	5.00	5.10	Model 19	4.90	5.20	5.50	5.80	6.10	6.40	6.70
Model 2	4.70	4.80	4.90	5.00	5.10	5.20	5.30	Model 20	5.10	5.40	5.70	6.00	6.30	6.60	6.90
Model 3	4.90	5.00	5.10	5.20	5.30	5.40	5.50	Model 21	2.40	2.80	3.20	3.60	4.00	4.40	4.80
Model 4	3.20	3.40	3.60	3.80	4.00	4.20	4.40	Model 22	2.60	3.00	3.40	3.80	4.20	4.60	5.00
Model 5	3.40	3.60	3.80	4.00	4.20	4.40	4.60	Model 23	2.80	3.20	3.60	4.00	4.40	4.80	5.20
Model 6	4.00	4.20	4.40	4.60	4.80	5.00	5.20	Model 24	3.00	3.40	3.80	4.20	4.60	5.00	5.40
Model 7	4.20	4.40	4.60	4.80	5.00	5.20	5.40	Model 25	3.20	3.60	4.00	4.40	4.80	5.20	5.60
Model 8	4.40	4.60	4.80	5.00	5.20	5.40	5.60	Model 26	3.40	3.80	4.20	4.60	5.00	5.40	5.80
Model 9	4.60	4.80	5.00	5.20	5.40	5.60	5.80	Model 27	3.60	4.00	4.40	4.80	5.20	5.60	6.00
Model 10	4.80	5.00	5.20	5.40	5.60	5.80	6.00	Model 28	3.80	4.20	4.60	5.00	5.40	5.80	6.20
Model 11	5.00	5.20	5.40	5.60	5.80	6.00	6.20	Model 29	4.00	4.40	4.80	5.20	5.60	6.00	6.40
Model 12	3.50	3.80	4.10	4.40	4.70	5.00	5.30	Model 30	4.20	4.60	5.00	5.40	5.80	6.20	6.60
Model 13	3.70	4.00	4.30	4.60	4.90	5.20	5.50	Model 31	4.40	4.80	5.20	5.60	6.00	6.40	6.80
Model 14	3.90	4.20	4.50	4.80	5.10	5.40	5.70	Model 32	4.60	5.00	5.40	5.80	6.20	6.60	7.00
Model 15	4.10	4.40	4.70	5.00	5.30	5.60	5.90	Model 33	4.80	5.20	5.60	6.00	6.40	6.80	7.20
Model 16	4.30	4.60	4.90	5.20	5.50	5.80	6.10	Model 34	5.00	5.40	5.80	6.20	6.60	7.00	7.40
Model 17	4.50	4.80	5.10	5.40	5.70	6.00	6.30	Model 35	5.20	5.60	6.00	6.40	6.80	7.20	7.60
Model 18	4.70	5.00	5.30	5.60	5.90	6.20	6.50								

The depth is relative to sea level, and the unit of the model is km/s.

our images are shallower than that of the Zhoucheng array. Generally, velocity images from the Qina, Pianjiao, and Zhoucheng arrays reveal clear along-strike variations in LVZs beneath the CHF in the Qina and Binchuan segments.

Discussion

Delay-time analyses of Binchuan airgun source and teleseismic earthquake

As an active source similar to the methane source, the Binchuan airgun source (blue star in Fig. 1b), consisting of four 2000 in^3 Bolt airguns, was established in 2011 at the Dayindian reservoir and has been in operation for more than ten years by means of fixed-point repeated excitation (Wang *et al.*, 2012, 2020; Zhang *et al.*, 2017; Luan *et al.*, 2022). During the deployment of line 1 and line 2 dense arrays, intensive excitation (349 shots) was carried out. From stacked waveform of the airgun source recorded on the line 2 dense array, we identify a zone of travel-time delay that has a width of ~5.0 km (Fig. 9a). This is consistent with the width obtained from body-wave tomography using the methane source, providing independent evidence of the shallow LVZ.

In addition to the airgun, we also conduct delay-time analyses of teleseismic earthquakes following Yang *et al.* (2020). Teleseismic waves can sample the structure beneath the array with a nearly vertical incident angle, and thus the travel times of *P* waves can be effective to reveal heterogeneous local structure (Cochran *et al.*, 2009; Share *et al.*, 2019; Yang *et al.*, 2020, 2021). We filter the teleseismic waveforms from 0.05 to 1.5 Hz and then manually pick all *P*-wave arrivals for 35 teleseismic earthquakes (Fig. 1) with good SNR. The travel times of the direct teleseismic *P* waves show clear variation across the array, with an obvious delay in stations from −1 to 1 km in the profile (Fig. 9b), which is completely consistent with the width obtained from the body-wave tomography beneath the line 1 dense array.

Overall, the body-wave tomography using the methane source and delay-time analyses can both reflect heterogeneous local structure beneath the dense arrays, and also depict the similar width of the LVZ. However, high-resolution body-wave tomography can also provide good constraints on the depth and actual velocity structure of the LVZ.

Comparative analysis of geometric features in LVZ

The earth's medium can produce stress accumulation and deformation because of tectonic stress. The fault zone is a relatively brittle area in the earth's medium, with a low-velocity

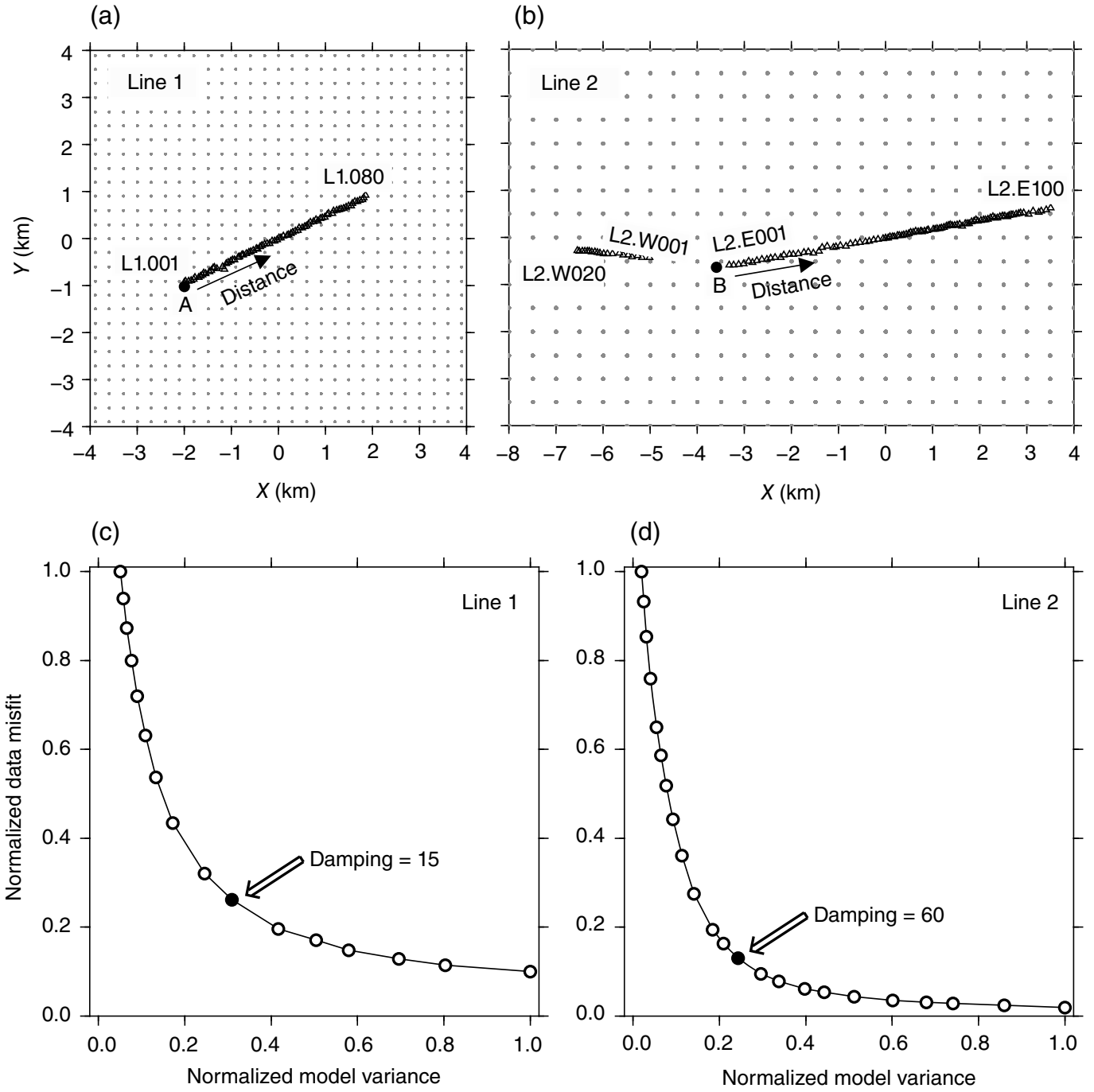

Figure 6. (a,b) Horizontal grid distribution and (c,d) selection of damping parameters during inversion for line 1 and line 2, respectively. Points A and B are the reference points for the horizontal coordinate (distance) in Figure 8.

distribution, which is more likely to conceive and produce earthquakes. The width of fault damage zones is usually on the order of 100 m (Li *et al.*, 1994, 2002, 2007; Peng *et al.*, 2003; Chester *et al.*, 2005; Sagy and Brodsky, 2009; Yang and Zhu, 2010; Ujiie *et al.*, 2013; Yang, 2015). For example, the width of LVZ beneath the Lavik lake fault for the 1999 M_w 7.1 Hector earthquake was about 75–100 m (Li *et al.*, 2002), and the 1992 M_w 7.3 Landers earthquake produced the LVZ of ~300 m width (Peng *et al.*, 2003; Li *et al.*, 2007). Some studies also showed much wider damage zones. For example, Cochran *et al.* (2009) obtained LVZs greater than 1 km in width on the Calico fault in California, which is located between the damage zones of the 1992 Landers and 1999 Hector earthquakes.

Several studies have also analyzed the velocity contrast between the inner and outer sides of the LVZ. The results of the fault zone trapped waves show that shear-wave velocities in the LVZ can be reduced by up to 20%–50% relative to the

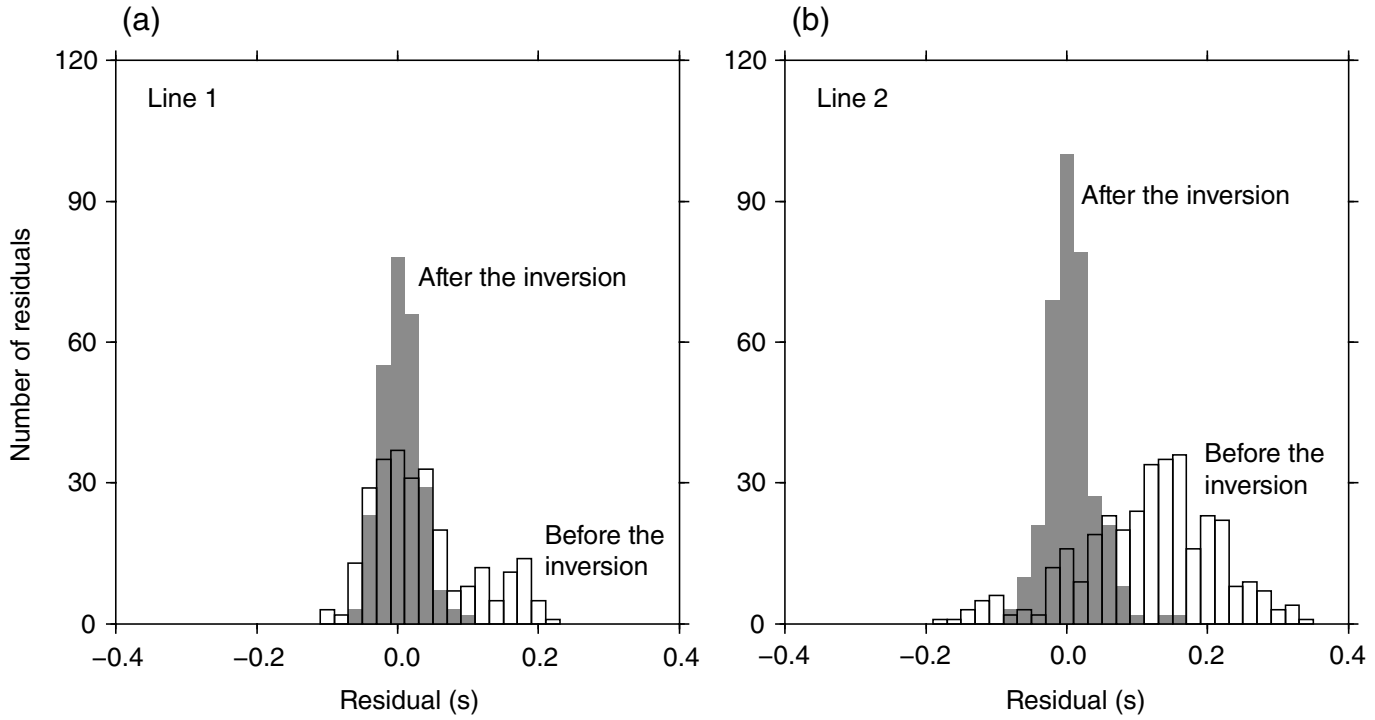

Figure 7. Travel-time residuals before (using the 1D initial model) and after (using the 3D model) tomographic inversion for the (a) line 1 and (b) line 2, respectively.

outside (Cochran *et al.*, 2009). Measurements of differential times and waveform modeling of head waves in the San Andreas fault's Bear Valley area also show a 20%–50% velocity contrast of LVZ (McGuire and Ben-Zion, 2005). In addition to the tens of percent velocity anomalies mentioned earlier, some studies show that the difference is relatively small. For example, Allam *et al.* (2014) and Yang *et al.* (2015) revealed a 3%–8% and 5%–8% velocity contrast along the Hayward fault and the 2010 M_w 6.9 Yushu earthquake ruptured zone, respectively, through the analysis and arrival-time difference between the head waves and direct *P* waves.

In the recent years, many studies have been conducted on the depth of LVZs. However, it is still controversial whether it extends to the base of the seismogenic zone or is only limited to the shallow layer. For example, Li and Vernon (2001) showed that the LVZ beneath the San Jacinto fault is as deep as 15–20 km, whereas Lewis *et al.* (2005) estimated it to be only 3–5 km deep. With the development of large-aperture dense arrays across faults, high-resolution imaging at Long Beach and the San Jacinto fault showed that the depth of LVZ only extends to the shallow part (Lin *et al.*, 2013; Schmandt and Clayton, 2013; Ben-Zion *et al.*, 2015; Share *et al.*, 2019).

Generally, seismic methods cannot distinguish whether the velocity reduction across the fault is caused by shallow sediment, fault damage zones, or other influencing factors (Yang *et al.*, 2020). In our study area, the CHF has a complex geological pattern and plays a significant role in controlling the tectonic geomorphology, velocity structure, and basin deposition of the shallow surface. In addition, no major earthquake has ever occurred in our dense array layout area (Fan *et al.*, 2006; Luo *et al.*, 2015; Huang *et al.*, 2018, 2021). Yang *et al.* (2020) used ambient noise tomography to obtain a distinct ~3.4 km wide and ~1.5 km depth LVZ (velocity reduced by 40%–60%) under the CHF beneath the Zhoucheng array, and interpreted the LVZ as loose Binchuan basin sediments. Therefore, we also interpreted the LVZ beneath the Qina and Pianjiao arrays as the sedimentary material controlled by the CHF, rather than the fault damaged zones that should be on a smaller scale in width.

Relationship between velocity anomaly and geomorphic distribution

The line 1 dense array was deployed along the Qina basin, where Holocene fluvial facies and flood-basal facies, Pleistocene lacustrine and fluvial deposits in the basin interior, Permian basalt on the west side of the basin, and Jurassic mudstone and sandstone on the east side of the basin were found, forming a high–low–high distribution trend of velocity anomalies (Fig. 8a). According to the previous studies, the deepest sedimentary thickness of the Qina basin can reach 700–800 m (Institute of Geology, China Earthquake Administration and Yunnan Earthquake Agency, 1990; Huang *et al.*, 2021), which is consistent with the distribution depth of low-velocity anomalies obtained by our imaging result (Fig. 8a). Huang *et al.* (2018, 2021) showed that a water system dislocation phenomenon is

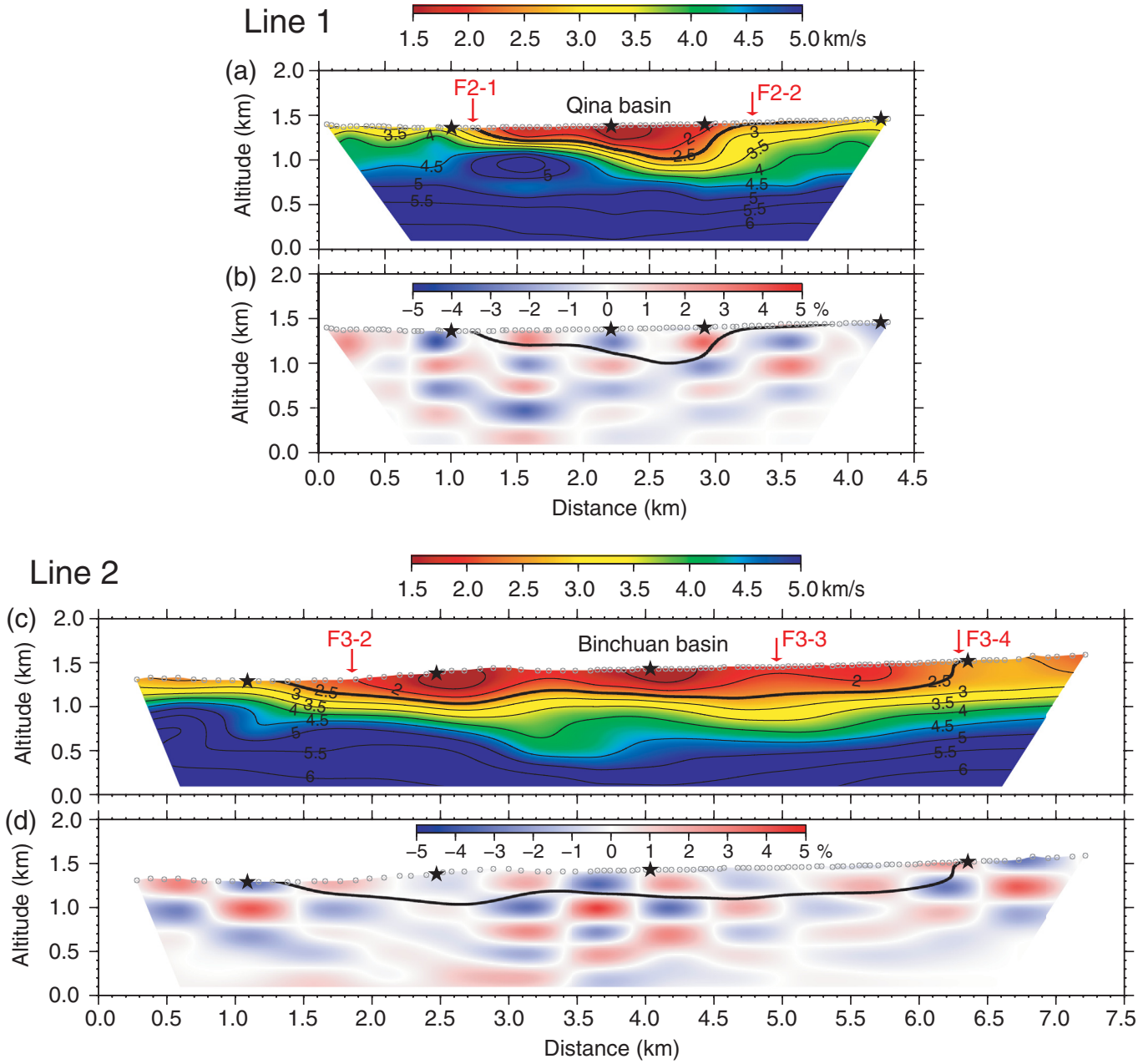

related to Quaternary activities around the Qina basin, and the cumulative left-lateral strike-slip displacement of the fault can reach 5–6 km. Because of the azimuth of the array layout, the width of the LVZ in this study is about 2 km.

The line 2 dense array is located in the Binchuan basin, slightly north of the BB′ profile in Luo *et al.* (2015), and the shallow velocity distribution is very consistent with the Quaternary sediments (Fig. 8c). The Dongshan Mountain is located on the east side of the Binchuan fault (F3-4), and it has a lithology of sandstone and mudstone dated in Triassic and Jurassic sandstone. The west side of the Hequ–Shangying fault (F3-2) is composed of Triassic sandstone and mudstone, as well as Permian basalt. These two areas above have relatively high velocities. Between the Hequ–Binju fault (F3-3) and the

Figure 8. (a,c) Results of the *P*-wave velocity structure and (b, d) checkerboard resolution test beneath the line 1 (Qina) dense array (0.3 km × 0.3 km × 0.25 km) and line 2 (Pianjiao) dense array (0.5 km × 0.5 km × 0.25 km). The altitude of the vertical axis is relative to sea level. The distance of the horizontal axis is the relative distance along the line 1 and line 2 to point A and point B in Figure 6, respectively. The black stars and gray dots represent the location of methane sources and dense array, respectively. The thick, solid line represents the contour line at 2.5 km/s to delineate the range of the *P*-wave low-velocity zone (LVZ). F2-1, Qina fault; F2-2, Jinjiang fault; F3-2, Hequ-Shangying fault; F3-3, Hequ-Binju fault; and F3-4, Binchuan fault.

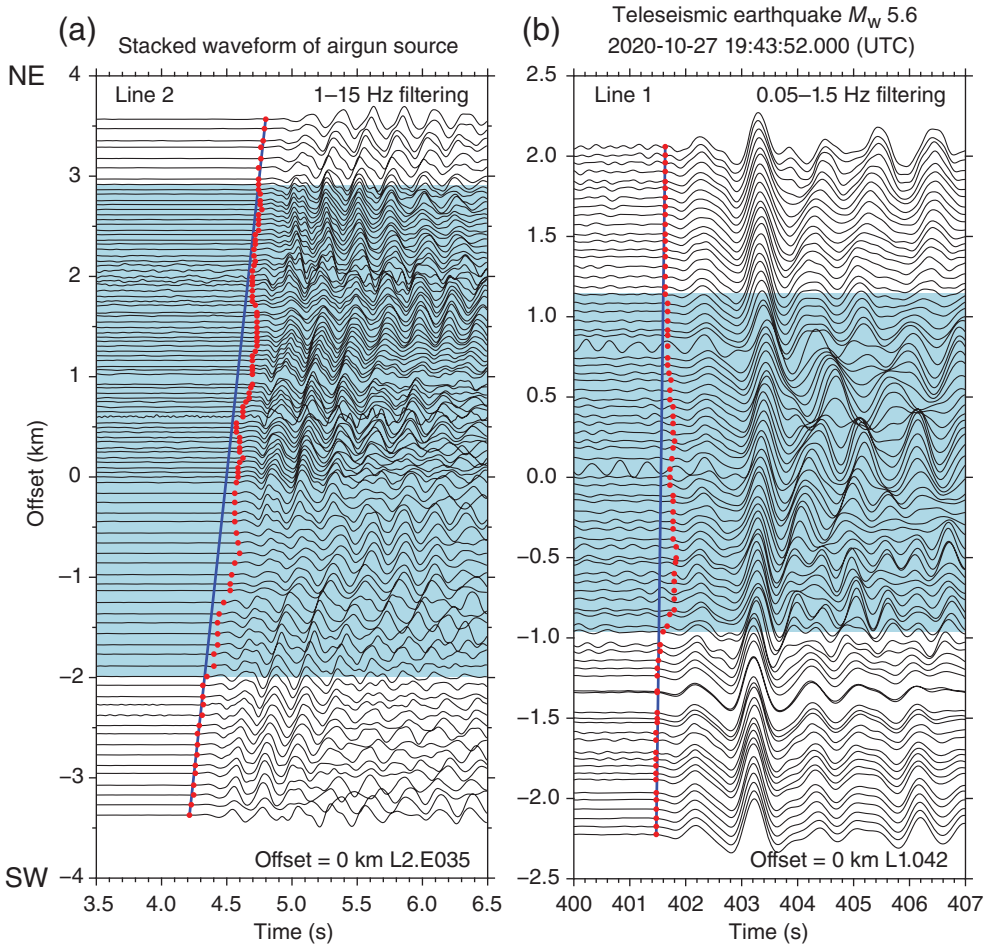

Figure 9. *P*-wave delay-time analyses of Binchuan airgun source (a, blue star in Fig. 1) and one teleseismic earthquake (b, purple dots in Fig. 1). The red dots represent the manually picked travel times. The waveforms are uniformly normalized across the array. *Y* axis shows the length of the array profile from southwest (SW) to northeast (NE). The blue shaded areas indicate the interpreted LVZs according to travel-time delays and waveform changes.

Binchuan fault (F3-4), there are Holocene fluvial and flood-based facies deposits showing a low-velocity anomaly. The area between the Hequ–Shangying fault (F3-2) and the Hequ–Binju fault (F3-3) is composed of Pleistocene lacustrine and fluvial deposits. These two faults also sandwich the Sheshan Formation block uplift, which is consistent with the low–high–low velocity distribution trend below the fault zone. In addition, several groups of imbricate-like small normal faults are also developed in these Early Pleistocene Sheshan Formation strata (Luo *et al.*, 2015). The imaging results continue to show low velocity, because some Pleistocene lacustrine and fluvial deposits still exist on the west side of the Hequ–Shangying fault (F3-2). Generally, the LVZ beneath line 2 gradually shallows on the west side and sharply decreases on the east side (Fig. 8c).

The line 2 dense array is mainly located in Pianjiao Street (Fig. 1) on the north side of the Lijiao deposition center. In geomorphology, the Binchuan fault (F3-4) affects the development of the Dongshan high mountains and multilevel piedmont large alluvial and proluvial fans, and controls the Lijiao deposition center together with the Hequ–Binju fault (F3-3) (Figs. 1 and 8c). The existing study (Institute of Geology, China Earthquake Administration and Yunnan Earthquake Agency, 1990; Luo *et al.*, 2015) shows that the maximum sedimentary thickness is about 500 m, which is consistent with the distribution depth of LVZ beneath line 2 in this study. The width of the LVZ beneath line 2 is about 5 km, which is slightly larger than the 3.4 km wide LVZ obtained by Yang *et al.* (2020), with a wider spread of sediments.

Formation mechanism and fault activity in the Qina and Binchuan basins

The distribution and shape characteristics of the basins in the NYRZ are related to the properties of fault structures (Huang *et al.*, 2014). The Qina basin is a long-axis near north–south-trending diamond-shaped rift basin formed by the tensile stress of a series of strike-slip faults, and the boundary faults on the northwest and southwest sides of the basin are small normal faults (Fig. 10a). The Binchuan basin is a crescent-shaped and jagged rift basin controlled by the Shangcang–Yupeng fault (F3-1) with obvious strike-slip properties on the west side and the Binchuan fault (F3-4) with obvious normal fault properties on the east side (Fig. 10a).

The length-to-minor axis ratio (LMAX) of the basin can reflect the intensity of fault activity. In addition, the height difference between the basin and the surrounding mountain (HDBM) can indicate the intensity of the fault vertical activity (Huang *et al.*, 2014). The basin is more likely to develop along the fault strike for the faults with strong activity, whereas the basin is more likely to widen because of the external dynamic action for the faults with weak activity. The LMAX and HDBM of the Qina basin affected by the strike-slip pull-out extension

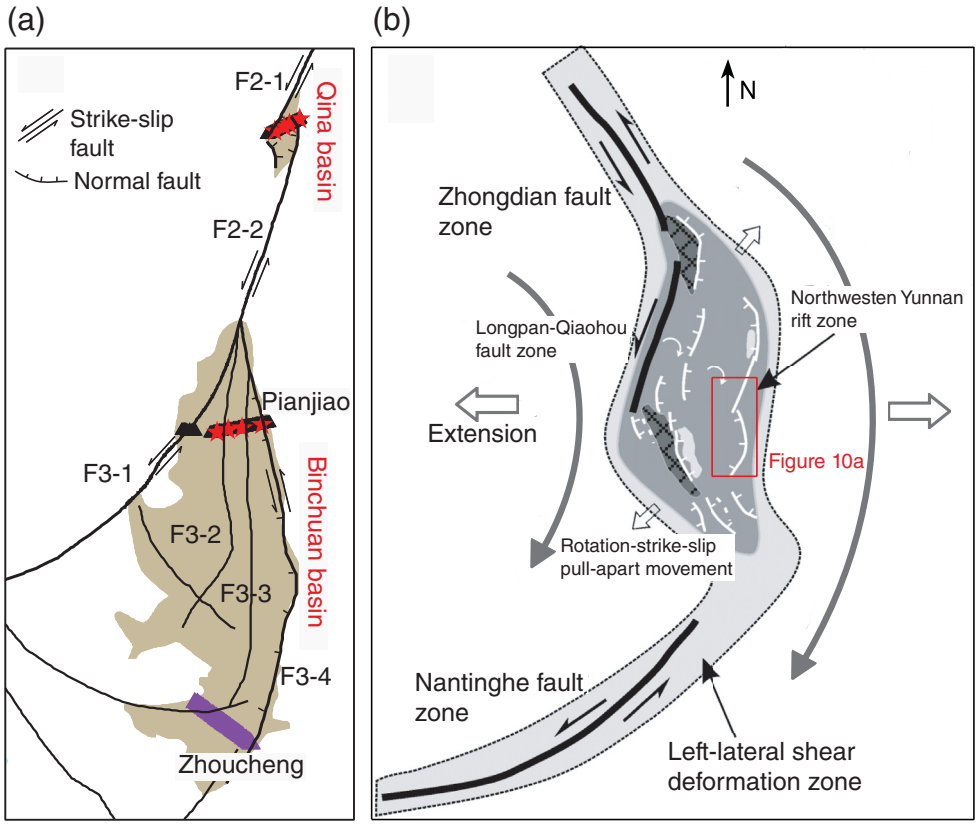

Figure 10. (a) Fault distribution and (b) formation mechanism of the Qina and Binchuan basins. The brownish areas represent the distribution range of Binchuan and Qina basins (Huang *et al.*, 2014). Panel (b) is modified from Wu *et al.* (2009). F2-1, Qina fault; F2-2, Jinjiang fault; F3-1, Shangcang-Yupeng fault; F3-2, Hequ-Shangying fault; F3-3, Hequ-Binju fault; and F3-4, Binchuan fault.

are 1.13 and 1441 m, whereas the LMAX and HDBM of the Binchuan composite faulted basin controlled by both strike-slip and normal faults are 1.91 and 1888 m, respectively (Huang *et al.*, 2014). Based on the dislocation of the water system and the HDBM, Huang *et al.* (2018) obtained the fault activity rate, and indicated that the vertical activity rate and strike-slip activity rate of the Qina (F2-1) and Jinjiang faults (F2-2) near the Qina basin are 0.41–0.45 mm/yr and 0.21–0.66 mm/yr since 5.0 Ma, respectively. In addition, the vertical activity rate of the northern segment of the Binchuan fault (F3-4) on the eastern boundary of the Binchuan basin is 0.51 mm/yr, and the strike-slip activity rate of the Shangcang-Yupeng fault (F3-1) on the western boundary is less than 0.36 mm/yr. In summary, the Quaternary activity of the CHF has obvious segmentation and spatial differences. The activity in the Binchuan basin is stronger than that in the Qina basin; however, the overall horizontal strike-slip activity decreases from north to south.

The active tectonic mechanism in the Qina and Binchuan basins is closely related to the movement pattern of the NYRZ (Wu *et al.*, 2009; Cheng *et al.*, 2012; Li *et al.*, 2012; Luo *et al.*, 2015). The Zhongdian fault zone, Longpan–Qiaohou fault zone, and Nantinghe fault zone with left-step strike-slip properties together constitute an arc-shaped left-lateral shear deformation zone (Fig. 10b), and the NYRZ is located in its pull-stage zone (Lacassin *et al.*, 1998; Luo *et al.*, 2015). The near north–south-trending normal faults are more active against the regional tectonic background of near the east–west extension. Simultaneously, the study area also exhibits an obvious left-lateral strike-slip effect, which makes it trend to the northeast because of the clockwise rotation of the northwestern microblock. For the Binchuan basin, the north–south-trending faults (F3-2 and F3-3) may start to turn due to clockwise rotation as early as in the Middle Pleistocene, and sedimentation controlled by the normal fault and the clockwise rotation of the fault may occur simultaneously. In addition, the left-lateral strike-slip action near the Binchuan basin is superimposed with the clockwise rotation action, forming a unique tectonic stress model in the region. A series of secondary depositional centers developed on the southcentral side of the basin, with a gradual increase in the distance between the Shangcang–Yupeng (F3-1) and Binchuan faults (F3-4) and the transition of the F3-4 fault to the northeast direction.

Generally, complex active tectonic systems in the Qina and Binchuan basins controlled by the CHF were formed under the combined action of the regional near east–west-trending extension and the clockwise rotation of microblocks, reflecting the left-lateral pull-apart movement pattern of the NYRZ under the overall clockwise rotation of the Qinghai–Tibet Plateau (Luo *et al.*, 2015).

Conclusions

In this study, we performed body-wave tomography based on the methane source signals recorded by the Qina and Pianjiao dense across-fault arrays beneath the CHF in Yunnan, China, and obtained the high-resolution shallow V_P structure beneath the arrays. Our tomographic results show that LVZs beneath the CHF have clear along-strike variations. The LVZs have widths of ~2 and ~5 km beneath the Qina and Pianjiao arrays,

respectively, and the velocity contrasts along the interface of the LVZ can reach 20%–50%. The LVZs extend to ~500 m in depth and are consistent with the Quaternary sediments, which were formed by the combined action of the regional near-east–west stretching and the clockwise rotation of the microblocks, controlled by the regional fault activity. Our results show that the high-resolution shallow velocity structure of the fault zone can be obtained using the sparse excitation of methane sources and short-period dense array observation.

Data and Resources

Waveform data and *P*-wave travel times of the methane sources used in this study are available at doi: 10.6084/m9.figshare.21090031.v2. Figures in this study were produced using the Generic Mapping Tools (GMT) software package (Wessel *et al.*, 2013).

Declaration of Competing Interests

The authors acknowledge that there are no conflicts of interest recorded.

Acknowledgments

The authors are grateful to Nanjing University and Dali Center, China Seismic Experimental Site for their hard work during the deployment of the dense arrays. The authors thank Zhonghai Wu and Xiaolong Huang for providing fault data near the Chenghai fault zone. The authors also thank the reviewers for their constructive comments that helped improve the article. This work was supported jointly by the Special Fund of the Institute of Geophysics, China Earthquake Administration (Grant Numbers DQJB19B32 and DQJB22R31), the National Natural Science Foundation of China (Grant Numbers 42104045, 41974069, and 42204053), Hong Kong Special Administrative Region (HKSAR) Research Grant Council General Research Fund (GRF) Grant Number 14306122, The Chinese University of Hong Kong (CUHK) Direct Grant from Faculty of Science, State Key Lab of Earthquake Dynamics (Grant Number LED2021B03).

References

Allam, A. A., Y. Ben-Zion, and Z. Peng (2014). Seismic imaging of a bimaterial interface along the Hayward fault, CA, with fault zone head waves and direct P arrivals, *Pure Appl. Geophys.* **171,** 2993–3011, doi: 10.1007/s00024-014-0784-0.

Ampuero, J. P., J. P. Vilotte, and F. Sanchez-Sesma (2002). Nucleation of rupture under slip dependent friction law: Simple models of fault zone, *J. Geophys. Res.* **107,** no. B12, 2324, doi: 10.1029/2001JB000452.

Barr, T. D., and G. A. Houseman (1992). Distribution of deformation around a fault in a non-linear ductile medium, *Geophys. Res. Lett.* **19,** no. 11, 1145–1148, doi: 10.1029/92GL00863.

Ben-Zion, Y., and P. Malin (1991). San Andreas fault zone head waves near Parkfield, California, *Science* **251,** no. 5001, 1592–1594, doi: 10.1126/science.251.5001.1592.

Ben-Zion, Y., and C. G. Sammis (2003). Characterization of fault zones, *Pure Appl. Geophys.* **160,** no. 3, 677–715, doi: 10.1007/PL00012554.

Ben-Zion, Y., F. L. Vernon, Y. Ozakin, D. Zigone, Z. E. Ross, H. Meng, M. White, J. Reyes, D. Hollis, and M. Barklage (2015). Basic data features and results from a spatially dense seismic array on the San Jacinto fault zone, *Geophys. J. Int.* **202,** no. 1, 370–380, doi: 10.1093/gji/ggv142.

Chen, Y., B. Wang, and H. Yao (2017). Seismic airgun exploration of continental crust structures, *Sci. China Earth Sci.* **60,** no. 10, 1739–1751, doi: 10.1007/s11430-016-9096-6.

Chen, Z., H. Yao, X. Shao, S. Luo, and H. Yang (2023). Detailed sedimentary structure of the Mianning segment of the Anninghe fault zone revealed by H/V spectral ratio, *Earthq. Res. Adv.* 10.1016/j.eqrea.2023.100232.

Cheng, J., X. Xu, W. Gan, W. Ma, W. Chen, and Y. Zhang (2012). Block model and dynamic implication from the earthquake activities and crustal motion in the southeastern margin of Tibetan plateau, *Chin. J. Geophys.* **55,** no. 4, 1198–1212, doi: 10.6038/j.issn.0001-5733.2012.04.016.

Chester, F. M., J. P. Evans, and R. L. Biegel (1993). Internal structure and weakening mechanisms of the San Andreas fault, *J. Geophys. Res.* **98,** 771–786, doi: 10.1016/0148-9062(93)92238-L.

Chester, J. S., F. M. Chester, and A. K. Kronenberg (2005). Fracture surface energy of the Punchbowl fault, San Andreas system, *Nature* **437,** no. 7055, 133–136, doi: 10.1038/nature03942.

Choi, J. H., P. Edwards, K. Ko, and Y. S. Kim (2016). Definition and classification of fault damage zones: A review and a new methodological approach, *Earth Sci. Rev.* **152,** 70–87, doi: 10.1016/j.earscirev.2015.11.006.

Choi, J. H., K. Jin, D. Enkhbayar, B. Davvasambuu, A. Bayasgalan, and Y. S. Kim (2012). Rupture propagation inferred from damage patterns, slip distribution, and segmentation of the 1957 MW8. 1 Gobi-Altay earthquake rupture along the Bogd fault, Mongolia, *J. Geophys. Res.* **117,** no. B12, doi: 10.1029/2011JB008676.

Cochran, E. S., Y. Li, P. M. Shearer, S. Barbot, Y. Fialko, and J. E. Vidale (2009). Seismic and geodetic evidence for extensive, long-lived fault damage zones, *Geology* **37,** no. 4, 315–318, doi: 10.1130/G25306A.1.

Dai, G., and Y. An (2020). China earthquake administration: Chinese seismic network, *Summary Bull. Int. Seismol. Centre* **54,** no. II, 28–40, doi: 10.31905/XWIVRBRI.

Deng, Q. D., P. Z. Zhang, Y. K. Ran, X. P. Yang, W. Min, and L. C. Chen (2003). Active tectonics and earthquake activities in China, *Earth Sci. Front.* **10,** no. S1, 66–73.

Denolle, M. A., H. Miyake, S. Nakagawa, N. Hirata, and G. C. Beroza (2014). Long-period seismic amplification in the Kanto Basin from the ambient seismic field, *Geophys. Res. Lett.* **41,** no. 7, 2319–2325, doi: 10.1002/2014GL059425.

Evans, J. P., and F. M. Chester (1995). Fluid-rock interaction in faults of the San Andreas system: inferences from San Gabriel fault rock geochemistry and microstructures, *J. Geophys. Res.* **100,** no. B7, 13,007–13,020.

Evans, J., D. Eberhart-Phillips, and C. H. Thurber (1994). User's manual for *SIMULPS12* for imaging Vp and Vp/Vs: A derivative of the "Thurber" tomographic inversion *SIMUL3* for local earthquakes and explosions, *U.S. Geol. Surv. Open-File Rept. 94–431*, available at https://pubs.usgs.gov/of/1994/0431/report.pdf (last accessed May 2023).

Fan, C., G. Wang, S. Wang, and E. Wang (2006). Structural interpretation of extensional deformation along the Dali fault system,

southeastern margin of the Tibetan plateau, *Int. Geol. Rev.* **48,** no. 4, 287–310, doi: 10.2747/0020-6814.48.4.287.

Fohrmann, M., H. Igel, G. Jahnke, and Y. Ben-Zion (2004). Guided waves from sources outside faults: An indication for shallow fault zone structure, *Pure Appl. Geophys.* **161,** 2125–2137, doi: 10.1007/s00024-004-2553-y.

Goebel, T. H. W., E. Hauksson, P. M. Shearer, and J. P. Ampuero (2015). Stress-drop heterogeneity within tectonically complex regions: A case study of San Gorgonio Pass, southern California, *Geophys. J. Int.* **202,** 514–528, doi: 10.1093/gji/ggv160.

Hillers, G., M. Campillo, Y. Ben-Zion, and P. Roux (2014). Seismic fault zone trapped noise, *J. Geophys. Res.* **119,** 5786–5799, doi: 10.1002/2014JB011217.

Huang, X., Z. Wu, X. Huang, F. Liu, and K. Wu (2021). Late Cenozoic transtensional deformation along the Chenghai fault zone and its constraint on micro-block clockwise rotation in southeastern Tibetan plateau, *Tectonics* doi: 10.1002/essoar.10506572.1.

Huang, X., Z. Wu, X. Huang, and R. Luo (2018). Tectonic geomorphology constrains on Quaternary activity and segmentation along Chenghai-Binchuan fault zone in northwest Yunnan, China, *Earth Sci.* **44,** no. 12, 4651–4670, doi: 10.3799/dqkx.2017.548.

Huang, X., Z. Wu, J. Li, C. Nima, Y. Liu, X. Huang, and Y. Zhang (2014). Tectonic geomorphology and Quaternary tectonic activity in the northwest Yunnan rift zone, *Geol. Bull. China* **33,** no. 4, 578–593, doi: 10.3969/j.issn.1671-2552.2014.04.013.

Huang, Y., and J. P. Ampuero (2011). Pulse-like ruptures induced by low-velocity fault zones, *J. Geophys. Res.* **116,** B12307, doi: 10.1029/2011JB008684.

Huang, Y., H. Li, X. Liu, Y. Zhang, M. Liu, Y. Guan, and J. Su (2020). The multiscale structure of the Longmen Shan central fault zone from local and teleseismic data recorded by short-period dense arrays, *Bull. Seismol. Soc. Am.* **110,** 3077–3087, doi: 10.1785/0120190292.

Institute of Geology, China Earthquake Administration and Yunnan Earthquake Agency (1990). *The Active Faults in Northwest Yunnan*, Seismological Press, Beijing, 321 pp, available at http://img.sslibrary.com/n/slib/book/slib/10392460/ff230ca0a54c46c78613a75041661a79/e5e08b180ce63f3fb9e74cb46b415e20.shtml?dxbaoku=false&moocbaoku=false&deptid=3064&fav=https%3A%2F%2Fwww.sslibrary.com%2Freader%2Fpdg%2Fpdgreader%3Fd%3Db6093dcaa5914ffb685238a3c3554c69%26ssid%3D10392460&fenlei=14050407&spage=1&t=5&username=124.17.4.51&view=-1 (last accessed May 2023).

Jiang, X. H., S. Q. Hu, and H. F. Yang (2021). Depth extent and Vp/Vs ratio of the Chenghai fault zone, Yunnan, China constrained from dense-array-based teleseismic receiver functions, *J. Geophys. Res.* **126,** e2021JB022190 , doi: 10.1029/2021JB022190.

Kahraman, M., D. G. Cornwell, D. A. Thompson, S. Rost, G. A. Houseman, N. Türkelli, U. Teoman, S. A. Poyraz, M. Utkucu, and L. Gülen (2015). Crustal-scale shear zones and heterogeneous structure beneath the North Anatolian fault zone, Turkey, revealed by a high-density seismometer array, *Earth Planet. Sci. Lett.* **430,** 129–139, doi: 10.1016/j.epsl.2015.08.014.

Kawase, H. (1996). The cause of the damage belt in Kobe: "The Basin-Edge Effect," constructive interference of the direct s-wave with the basin-induced diffracted/Rayleigh waves, *Seismol. Res. Lett.* **67,** no. 5, 25–34, doi: 10.1785/gssrl.67.5.25.

Kissling, E. (1995). Velest user's guide, *Internal Rept. 26*, Institute of Geophysics, ETH Zurich, Zürich, Switzerland, available at https://www.researchgate.net/publication/284401265_Velest_User's_Guide (last accessed May 2023).

Kissling, E., W. L. Ellsworth, D. Eberhart-Phillips, and U. Kradolfer (1994). Initial reference models in local earthquake tomography, *J. Geophys. Res.* **99,** no. B10, 19,635–19,646.

Kurzon, I., F. L. Vernon, Y. Ben-Zion, and G. Atkinson (2014). Ground motion prediction equations in the San Jacinto fault zone: Significant effects of rupture directivity and fault zone amplification, *Pure Appl. Geophys.* **171,** 3045–3081, doi: 10.1007/s00024-014-0855-2.

Lacassin, R., A. Replumaz, and P. H. Leloup (1998). Hairpin river loops and slip-sense inversion on southeast Asian strike-slip faults, *Geology* **26,** no. 8, 703–706.

Lewis, M., and Y. Ben-Zion (2010). Diversity of fault zone damage and trapping structures in the Parkfield section of the San Andreas fault from comprehensive analysis of near fault seismograms, *Geophys. J. Int.* **183,** 1579–1595.

Lewis, M. A., Y. Ben-Zion, and J. J. McGuire (2007). Imaging the deep structure of the San Andreas fault south of Hollister with joint analysis of fault zone head and direct P arrivals, *Geophys. J. Int.* **169,** no. 3, 1028–1042.

Lewis, M. A., Z. G. Peng, Y. Ben-Zion, and F. L. Vernon (2005). Shallow seismic trapping structure in the San Jacinto fault zone near Anza, California, *Geophys. J. Int.* **162,** 867–881, doi: 10.1111/j.1365-246X.2005.02684.x.

Li, B., and A. Ghosh (2016). Imaging rupture process of the 2015 Mw 8.3 Illapel earthquake using the US Seismic array, *Pure Appl. Geophys.* **173,** 2245–2255, doi: 10.1007/s00024-016-1323-y.

Li, H., H. Wang, Z. Xu, J. Si, J. Pei, F. Li, Y. Huang, S. Song, L. Kuo, Z. Sun, M. Chevalier, and D. Liu (2013). Characteristics of the fault-related rocks, fault zones and the principal slip zone in the Wenchuan earthquake fault Scientific Drilling Project Hole-1 (WFSD-1), *Tectonophysics* **584,** 23–42, doi: 10.1016/j.tecto.2012.08.021.

Li, H., L. Zhu, and H. Yang (2007). High-resolution structures of the landers fault zone inferred from aftershock waveform data, *Geophys. J. Int.* **171,** no. 3, 1295–1307, doi: 10.1111/j.1365-246X.2007.03608.x.

Li, S. H., B. C. Huang, and R. X. Zhu (2012). Paleomagnetic constraints on the tectonic rotation of the southeastern margin of the Tibetan plateau, *Chin. J. Geophys.* **55,** no. 1, 76–94.

Li, Y., K. Aki, D. Adams, and A. Hasemi (1994). Seismic guided waves trapped in the fault zone of the Landers, California, earthquake of 1992, *J. Geophys. Res.* **99,** no. B6, 11,705–11,722, doi: 10.1029/94JB00464.

Li, Y., P. Leary, K. Aki, and P. Malin (1990). Seismic trapped modes in the Oroville and San Andreas fault zones, *Science* **249,** no. 4970, 763–766, doi: 10.1126/science.249.4970.763.

Li, Y., J. E. Vidale, S. M. Day, D. D. Oglesby, and , and the SCEC Field Working Team (2002). Study of the 1999 *M* 7.1 Hector Mine, California, earthquake fault plane by trapped waves, *Bull. Seismol. Soc. Am.* **92,** no. 4, 1318–1332, doi: 10.1785/0120000909.

Li, Y. G., and F. L. Vernon (2001). Characterization of the San Jacinto fault zone near Anza, California, by fault zone trapped waves, *J. Geophys. Res.* **106,** 30671–30688, doi: 10.1029/2000JB000107.

Lin, F. C., D. Z. Li, R. W. Clayton, and D. Hollis (2013). High-resolution 3D shallow crustal structure in Long Beach, California: Application of ambient noise tomography on a dense seismic array, *Geophysics* **78,** no. 4, Q45–Q56, doi: 10.1190/GEO2012-0453.1.

Lin, G. Q., P. M. Shearer, R. S. Matoza, P. G. Okubo, and F. Amelung (2014). Three-dimensional seismic velocity structure of Mauna Loa and Kilauea volcanoes in Hawaii from local seismic tomography, *J. Geophys. Res.* **119,** no. 5, 4377–4392, doi: 10.1002/2013JB010820.

Liu, C., H. Yang, B. Wang, and J. Yang (2021). Impacts of reservoir water level fluctuation on measuring seasonal seismic travel time changes in the Binchuan basin, Yunnan, China, *Remote Sens.* **13,** no. 12, 2421, doi: 10.3390/rs13122421.

Luan, Y., H. Yang, B. Wang, W. Yang, W. Wang, J. Yang, and X. Li (2022). Time-lapse monitoring of daily velocity changes in Binchuan, southwestern China, using large volume air gun source array data, *Seismol. Res. Lett.* **93,** no. 2A, 914–930, doi: 10.1785/0220210160.

Luan, Y., H. Yang, B. Wang, W. Yang, W. Wang, J Yang, X. Li, and J. Ran (2023). Seasonal variations of seismic travel-time changes in Binchuan, southwestern China, inferred from large volume air-gun source array data, *Seismol. Res. Lett.* **94,** no. 3, 1613–1626, doi: 10.1785/0220220200.

Luo, R. J., Z. H. Wu, X. L. Huang, X. J. Huang, C. J. Zhou, and T. T. Tian (2015). The main active faults and the active tectonic system of Binchuan area, northwestern Yunnan, *Geol. Bull. China* **34,** no. 1, 155–170, doi: 10.3969/j.issn.1671-2552.2015.01.013.

Manighetti, I., M. Campillo, S. Bouley, and F. Cotton (2007). Earthquake scaling, fault segmentation, and structural maturity, *Earth Planet. Sci. Lett.* **253,** nos. 3/4, 429–438, doi: 10.1016/j.epsl.2006.11.004.

Manighetti, I., G. King, and C. G. Sammis (2004). The role of off-fault damage in the evolution of normal faults, *Earth Planet. Sci. Lett.* **217,** nos. 3/4, 399–408, doi: 10.1016/S0012-821X(03)00601-0.

Manighetti, I., D. Zigone, M. Campillo, and F. Cotton (2009). Self-similarity of the largest-scale segmentation of the faults: Implications for earthquake behavior, *Earth Planet. Sci. Lett.* **288,** nos. 3/4, 370–381, doi: 10.1016/j.epsl.2009.09.040.

Matrullo, E., R. De Matteis, C. Satriano, O. Amoroso, and A. Zollo (2013). An improved 1-D seismic velocity model for seismological studies in the Campania–Lucania region (southern Italy), *Geophys. J. Int.* **195,** no. 1, 460–473, doi: 10.1093/gji/ggt224.

McGuire, J., and Y. Ben-Zion (2005). High-resolution imaging of the Bear Valley section of the San Andreas fault at seismogenic depths with fault-zone head waves and relocated seismicity, *Geophys. J. Int.* **163,** 152–164, doi: 10.1111/j.1365-246X.2005.02703.x.

Meng, H., and W. Fan (2021). Immediate foreshocks indicating cascading rupture developments for 527 M 0.9 to 5.4 Ridgecrest earthquakes, *Geophys. Res. Lett.* **48,** e2021GL095704 , doi: 10.1029/2021GL095704.

Peng, Z., Y. Ben-Zion, A. J. Michael, and L. Zhu (2003). Quantitative analysis of seismic fault zone waves in the rupture zone of the landers, 1992, California earthquake: Evidence for a shallow trapping structure, *Geophys. J. Int.* **155,** no. 3, 1021–1041, doi: 10.1111/j.1365-246X.2003.02109.x.

Perrin, C., I. Manighetti, J. P. Ampuero, F. Cappa, and Y. Gaudemer (2016). Location of largest earthquake slip and fast rupture controlled by along-strike change in fault structural maturity due to fault growth, *J. Geophys. Res.* **121,** no. 5, 3666–3685, doi: 10.1002/2015JB012671.

Qin, L., Y. Ben-Zion, H. Qiu, P.-E. Share, Z. E. Ross, and F. L. Vernon (2018). Internal structure of the San Jacinto fault zone in the trifurcation area southeast of Anza, California, from data of dense seismic arrays, *Geophys. J. Int.* **213,** no. 1, 98–114, doi: 10.1093/gji/ggx540.

Qin, L., P.-E. Share, H. Qiu, A. A. Allam, F. L. Vernon, and Y. Ben-Zion (2021). Internal structure of the San Jacinto fault zone at the Ramona Reservation, north of Anza, California, from dense array seismic data, *Geophys. J. Int.* **224,** no. 2, 1225–1241, doi: 10.1093/gji/ggaa482.

Qiu, H., Y. Ben-Zion, R. Catchings, M. R. Goldman, A. A. Allam, and J. Steidl (2021). Seismic imaging of the Mw 7.1 Ridgecrest earthquake rupture zone from data recorded by dense linear arrays, *J. Geophys. Res.* **126,** e2021JB022043, doi: 10.1029/2021JB022043.

Qiu, H., F. Niu, and L. Qin (2021). Denoising surface waves extracted from ambient noise recorded by 1-D linear array using three-station interferometry of direct waves, *J. Geophys. Res.* **126,** no. 8, e2021JB021712, doi: 10.1002/essoar.10505172.1.

Rosset, P., A. Bent, S. Halchuk, and L. Chouinard (2022). Positive correlation between dyfi intensity data and microzonation site classes for Ottawa, Quebec City, and the metropolitan area of Montreal, *Seismol. Res. Lett.* **93,** no. 6, 3468–3480, doi: 10.1785/0220220144.

Rost, S., G. A. Houseman, A. W. Frederiksen, D. G. Cornwell, M. Kahraman, S. Altuncu Poyraz, U. M. Teoman, D. A. Thompson, N. Türkelli, L. Gülen, M. Utkucu, and T. J. Wright (2021). Structure of the northwestern North Anatolian fault zone imaged via teleseismic scattering tomography, *Geophys. J. Int.* **227,** no. 2, 922–940, doi: 10.1093/gji/ggab265.

Sagy, A., and E. Brodsky (2009). Geometric and rheological asperities in an exposed fault zone, *J. Geophys. Res.* **114,** no. B2, doi: 10.1029/2008JB005701.

Schmandt, B., and R. W. Clayton (2013). Analysis of teleseismic P waves with a 5200-station array in Long Beach, California: Evidence for an abrupt boundary to inner borderland rifting, *J. Geophys. Res.* **118,** 5320–5338, doi: 10.1002/jgrb.50370.

Shao, X. H., H. J. Yao, Y. Liu, H. F. Yang, B. F. Tian, and L. H. Fang (2022). Shallow crustal velocity structures revealed by active source tomography and fault activities of the Mianning–Xichang segment of the Anninghe fault zone, southwest China, *Earth Planet. Phys.* **6,** no. 2, 204–213, doi: 10.26464/epp2022010.

Share, P.-E., A. A. Allam, Y. Ben-Zion, F. C. Lin, and F. L. Vernon (2019). Structural properties of the San Jancinto fault zone at Blackburn Saddle from seismic data of a dense linear array, *Pure Appl. Geophys.* **176,** no. 3, 1169–1191, doi: 10.1007/s00024-018-1988-5.

Share, P.-E., H. Qiu, F. L. Vernon, A. A. Allam, Y. Fialko, and Y. Ben-Zion (2022). General seismic architecture of the southern San Andreas fault zone around the Thousand Palms Oasis from a large-N nodal array, *Seismic Records* **2,** no. 1, 50–58, doi: 10.1785/0320210040.

She, Y., H. Yao, H. Yang, J. Wang, and J. Feng (2022). Constraining the depth extent of low-velocity zone along the Chenghai fault by dense array ambient noise interferometry and horizontal-to-vertical spectral ratio, *Tectonophysics* **827,** 229,265, doi: 10.1016/j.tecto.2022.229265.

Song, J., and H. Yang (2022). Seismic site response inferred from records at a dense linear array across the Chenghai fault zone, Binchuan, Yunnan, *J. Geophys. Res.* **127,** e2021JB022710, doi: 10.1029/2021JB022710.

Taylor, G., S. Rost, G. A. Houseman, and G. Hillers (2019). Near-surface structure of the North Anatolian fault zone from Rayleigh and Love wave tomography using ambient seismic noise, *Solid Earth* **10,** no. 2, 363–378, doi: 10.5194/se-10-363-2019.

Thurber, C. H. (1983). Earthquake locations and three-dimensional crustal structure in the Coyote Lake Area, central California, *J. Geophys. Res.* **88,** no. B10, 8226–8236, doi: 10.1029/JB088iB10p08226.

Thurber, C. H. (1993). Local earthquake tomography: Velocities and Vp/Vs-theory, in *Seismic Tomography: Theory and Practice*, H. M. Iyer and K. Hirahara (Editors), Chapman and Hall, London, 563–583.

Thurber, C. H., and D. Eberhart-Phillips (1999). Local earthquake tomography with flexible gridding, *Comput. Geosci.* **25,** no. 7, 809–818, doi: 10.1016/s0098-3004(99)00007-2.

Ujiie, K., H. Tanaka, T. Saito, A. Tsutsumi, J. J. Mori, J. Kameda, E. E. Brodsky, F. M. Chester, N. Eguchi, S. Toczko, *et al.* (2013). Low coseismic shear stress on the Tohoku-Oki megathrust determined from laboratory experiments, *Sciences* **342,** no. 6163, 1211–1214, doi: 10.1126/science.1243485.

Wang, B., H. Ge, B. Wang, H. Wang, Y. Zhang, H. Cai, and Y. Chen (2016). Practices and advances in exploring the subsurface structure and its temporal evolution with repeatable artificial sources, *Earthq. Res. China* **30,** no. 3, 284–297.

Wang, B., H. Ge, W. Yang, and W. Wang (2012). Transmitting seismic station monitors fault zone at depth, *Eos Trans. AGU*, **93,** no. 5, 49–56, doi: 10.1029/2012EO050001.

Wang, B., W. Yang, W. Wang, J. Yang, X. Li, and B. Ye (2020). Diurnal and semidiurnal P- and S-wave velocity changes measured using an Airgun source, *J. Geophys. Res.* **125,** e2019JB018218, doi: 10.1029/2019JB018218.

Wang, W., X. Wang, C. Meng, S. Dong, Z. Wang, J. Xie, B. Wang, W. Yang, S. Xu, and T. Wang (2019). Characteristics of the seismic waves from a new active source based on methane gaseous detonation, *Earthq. Res. China* **33,** no. 2, 354–366.

Weng, H., H. Yang, Z. Zhang, and X. Chen (2016). Earthquake rupture extents and coseismic slips promoted by damaged fault zones, *J. Geophys. Res.* **121,** no. 6, 4446–4457, doi: 10.1002/2015JB012713.

Wessel, P., W. H. F. Smith, R. Scharroo, J. Luis, and F. Wobbe (2013). Generic mapping tools: improved version released, *Eos Trans. AGU* **94,** no. 45, 409–410, doi: 10.1002/2013EO450001.

Wilson, J. E., J. S. Chester, and F. M. Chester (2003). Microfracture analysis of fault growth and wear processes, Punchbowl fault, San Andreas system, California, *J. Struct. Geol.* **25,** no. 11, 1855–1873, doi: 10.1016/S0191-8141(03)00036-1.

Wu, Z. H., Y. S. Zhang, D. G. Hu, X. T. Zhao, and P. S. Ye (2009). Late Quaternary normal faulting and its kinematic mechanism of eastern piedmont fault of the Haba–Yulong Snow Mountains in northwestern Yunnan, China, *Sci. China, Ser. D Earth Sci.* **52,** no. 10, 1470–1484, doi: 10.1007/s11430-009-0148-2.

Xu, S., W. Wang, W. Xu, L. Wang, X. Ma, X. Wang, C. Meng, and W. Yang (2021). Performance study of methane gas explosion source and its application in exploring of Hualong fault in Guangdong-Hong Kong-Macao Greater Bay area, *Chin. J. Geophys.* **64,** no. 12, 4269–4279, doi: 10.6038/cjg2021P0281.

Yang, H. (2015). Recent advances in imaging crustal fault zones: a review, *Earthq. Sci.* **28,** no. 2, 151–162, doi: 10.1007/s11589-015-0114-3.

Yang, H., and L. Zhu (2010). Shallow low-velocity zone of the San Jacinto fault from local earthquake waveform modelling, *Geophys. J. Int.* **183,** no. 1, 421–432, doi: 10.1111/j.1365-246X.2010.04744.x.

Yang, H., Y. Duan, J. Song, X. Jiang, X. Tian, W. Yang, W. T. Wang, and J. Yang (2020). Fine structure of the Chenghai fault zone, Yunnan, China, constrained from teleseismic travel time and ambient noise tomography, *J. Geophys. Res.* **125,** e2020JB019565, doi: 10.1029/2020JB019565.

Yang, H., Y. Duan, J. Song, W. Yang, W. Wang, X. Tian, and B. Wang (2021). Illuminating high-resolution crustal fault zones and temporal changes using multi-scale dense arrays and airgun sources, *Earthq. Res. Adv.* **1,** 100,001, doi: 10.1016/j.eqrea.2021.100001.

Yang, H., Z. Li, Z. Peng, Y. Ben-Zion, and F. Vernon (2014). Low-velocity zones along the San Jacinto Fault, Southern California, from body waves recorded in dense linear arrays, *J. Geophys. Res.* **119,** 8976–8990, doi: 10.1002/2014JB011548.

Yang, W., Z. G. Peng, B. S. Wang, Z. F. Li, and S. Y. Yuan (2015). Velocity contrast along the rupture zone of the 2010 Mw6.9 Yushu, China, earthquake from fault zone head waves, *Earth Planet. Sci. Lett.* **416,** 91–97, doi: 10.1016/j.epsl.2015.01.043.

Zhang, Y., H. Li, Y. Huang, M. Liu, Y. Guan, J. Su, and T. Wang (2019). Shallow structure of the Longmen Shan fault zone from a high-density, short-period seismic array, *Bull. Seismol. Soc. Am.* **110,** 38–48, doi: 10.1785/0120190147.

Zhang, Y. P., X. B. Li, W. T. Wang, B. S. Wang, B. Ye, J. Yang, and B. Wang (2017). Data service system and data quality assessment for mobile observation of transmitting seismic stations in Binchuan, Yunnan, *J. Seismol. Res.* **40,** no. 4, 525–533.

Zhang, Y. P., B. S. Wang, G. Q. Lin, Y. P. Ouyang, T. Wang, S. H. Xu, L. L. Song, and R. C. Wang (2020). Three-dimensional P-wave velocity structure of the Zhuxi ore deposit, South China revealed by control-source first-arrival tomography, *Minerals* **10,** 148, doi: 10.3390/min10020148.

Zhang, Y. P., B. S. Wang, T. Xu, W. Yang, W. T. Wang, Y. H. Xu, and L. Li (2020). Three-dimensional crustal Vp and Vs structures beneath the southern segment of the Tan-Lu fault revealed by active source and earthquake data, *Geophys. J. Int.* **223,** no. 3, 2148–2165, doi: 10.1093/gji/ggaa314.

Zhang, Y. P., W. T. Wang, W. Yang, M. Liu, J. B. Su, X. B. Li, and J. Yang (2021). Three-dimensional velocity structure around the focal area of the 2021 M_S 6.4 Yangbi earthquake, *Earthq. Sci.* **34,** no. 5, 399–412, doi: 10.29382/eqs-2021-0033.

Zhang, Z., Y. Deng, H. Qiu, Z. Peng, and J. Liu-Zeng (2022). High-resolution imaging of fault zone structure along the creeping section of the Haiyuan fault, NE Tibet, from data recorded by dense seismic arrays, *J. Geophys. Res.* **127,** e2022JB024468, doi: 10.1029/2022JB024468.

Zigone, D., Y. Ben-Zion, M. Lehujeur, M. Campillo, G. Hillers, and F. L. Vernon (2019). Imaging subsurface structures in the San Jacinto fault zone with high-frequency noise recorded by dense linear arrays, *Geophys. J. Int.* **217,** no. 2, 879–893, doi: 10.1093/gji/ggz069.

Manuscript received 8 February 2023
Published online 9 June 2023